Magnetic characteristics of high-speed jets in the Earth's magnetosheath

Master's Thesis
University of Turku
Dept. of Physics and Astronomy
Physics
February 2020
B.Sc. Laura Vuorinen
Reviewed by:
Docent Heli Hietala
Professor Rami Vainio

The originality of this thesis has been checked in accordance with the University of Turku quality assurance system using Turnitin OriginalityCheck service.

UNIVERSITY OF TURKU
Department of Physics and Astronomy
VUORINEN, LAURA Magnetic characteristics of high-speed jets in the Earth's magnetosheath
Master's Thesis, 63 p.
Physics
February 2020
The originality of this thesis has been checked in accordance with the University of Turku quality assurance system using the Turnitin OriginalityCheck service.

The solar wind plasma flows around the magnetosphere in the magnetosheath, downstream of the Earth's bow shock. Within the magnetosheath, jets with higher earthward velocities than their surroundings are often observed. These jets can trigger many types of effects when impacting the magnetopause, the boundary of the magnetosphere. Lately, observations have linked jets to triggering magnetic reconnection, which connects the solar wind's interplanetary magnetic field (IMF) with the Earth's magnetic field and allows solar wind mass and energy to enter the magnetosphere. Magnetic reconnection is efficiently driven during southward IMF, when the IMF is anti-parallel to the Earth's northward field at the subsolar magnetopause. In this thesis, we statistically study how the IMF orientation controls where jets occur and how often they impact the subsolar magnetopause, and whether jets could statistically affect magnetopause reconnection.

We use measurements from the Time History of Events and Macroscale Interactions during Substorms (THEMIS) satellites and from the OMNI solar wind data set from the years 2008–2011. We find that jets are 9 times more common downstream of the quasi-parallel shock, where the local shock normal is almost parallel with the IMF, than downstream of the quasi-perpendicular shock. Jets larger than 1 Earth radius are estimated to hit the subsolar magnetopause 5–60 times per hour depending on the IMF orientation. During northward IMF, jets exhibit southward fields close to the magnetopause more often than the non-jet magnetosheath. This suggests that the magnetic field within jets is statistically favorable for enhancing reconnection during the more quiet northward IMF conditions.

These results highlight the role of magnetosheath jets in the transport of solar wind energy into the magnetosphere. Impacts and the effects of jets are estimated to be very common downstream of the quasi-parallel shock. Magnetopause reconnection is a key process in space weather and jets are expected to enhance this process when it is generally suppressed. In the future, it is important to investigate the physical mechanisms behind these results and how often jets actually trigger magnetopause reconnection.

Keywords: space physics, magnetosheath, magnetosheath jets, magnetosphere, interplanetary magnetic field, solar wind, magnetic reconnection

TURUN YLIOPISTO
Fysiikan ja tähtitieteen laitos
VUORINEN, LAURA Maan magnetosfäärin pyörteisen välivyöhykkeen suihkuvirtausten magneettiset ominaisuudet

Pro gradu, 63 s.
Fysiikka
Helmikuu 2020
Turun yliopiston laatujärjestelmän mukaisesti tämän julkaisun alkuperäisyys on tarkastettu Turnitin Originality Check -järjestelmällä.

Aurinkotuulen plasma virtaa Maan magnetosfäärin ohi keulashokin alavirrassa sijaitsevassa pyörteisessä välivyöhykkeessä, jossa havaitaan usein ympäröivää plasmaa nopeampia suihkuvirtauksia. Nämä suihkuvirtaukset voivat aiheuttaa monenlaisia prosesseja törmätessään magnetosfäärin reunaan, magnetopausiin. Viime aikoina suihkuvirtaukset on liitetty magneettisen rekonnektion kytkemiseen magnetopausilla. Rekonnektiossa aurinkotuulen planeettainvälinen magneettikenttä (IMF) yhdistyy Maan magneettikentän kanssa mahdollistaen aurinkotuulen ja sen energian virtauksen magnetosfääriin. Tämä prosessi on erityisen yleinen IMF:n ollessa eteläinen eli vastakkaissuuntainen Maan kentän kanssa. Tässä tutkielmassa tutkitaan IMF:n suunnan vaikutusta suihkuvirtausten esiintyvyyteen ja siihen kuinka usein ne törmäävät magnetopausiin, sekä suihkuvirtausten mahdollista tilastollista vaikutusta magnetopausin rekonnektioon.

Tutkielmassa käytetään Time History of Events and Macroscale Interactions during Substorms -satelliittien (THEMIS) ja OMNI-aurinkotuuliaineiston mittauksia vuosilta 2008–2011. Tutkielman tulosten mukaan pitkittäisen keulashokin, missä IMF ja shokin normaali ovat lähes pitkittäiset, alavirrassa suihkuvirtauksia havaitaan 9 kertaa useammin kuin poikittaisen shokin alavirrassa. Maan sädettä suurempia suihkuvirtauksia arvioidaan törmäävän tutkittavaan magnetopausiin 5–60 kertaa tunnissa riippuen IMF:n suunnasta. Pohjoisen IMF:n aikaan suihkuvirtauksissa on magnetopausin lähellä selvästi useammin eteläistä magneettikenttää kuin normaalisti, eli niiden magneettikenttä on tällöin tilastollisesti suotuisa lisäämään rekonnektiota.

Tutkielman tulokset korostavat pyörteisen välivyöhykkeen suihkuvirtausten roolia aurinkotuulen energian välittämisessä magnetosfääriin. Suihkuvirtauksien törmäysten magnetopausiin, ja siten myös niiden vaikutusten, arvioidaan olevan todella yleisiä pitkittäisen shokin alavirrassa. Magnetopausin rekonnektio on keskeinen prosessi avaruussäässä, ja suihkuvirtausten voidaan odottaa lisäävän tätä rauhallisemman pohjoisen IMF:n aikaan. Jatkossa on tärkeää tutkia fysikaalisia mekanismeja näiden tulosten taustalla ja sitä kuinka yleistä suihkuvirtausten kytkemä magnetopausin rekonnektio todellisuudessa on.

Asiasanat: avaruusfysiikka, pyörteinen välivyöhyke, pyörteisen välivyöhykkeen suihkuvirtaukset, magnetosfääri, planeettainvälinen magneettikenttä, aurinkotuuli, magneettinen rekonnektio

Contents

Acronyms and abbreviations

AU	astronomical unit
BS	bow shock
CDF	cumulative distribution function
CIR	co-rotating interaction region
CME	coronal mass ejection
ESA	Electrostatic Analyzer/European Space Agency
FGM	Fluxgate Magnetometer
FTE	flux transfer event
GIPM	Geocentric Interplanetary Medium coordinate system
GPE	Geocentric Plasma Ecliptic coordinate system
GSE	Geocentric Solar Ecliptic coordinate system
GSM	Geocentric Solar Magnetospheric coordinate system
HCS	heliospheric current sheet
IMF	interplanetary magnetic field
IMP	Interplanetary Monitoring Platform spacecraft
KS2	two-sample Kolmogorov-Smirnov test
MHD	magnetohydrodynamics
MP	magnetopause
MSH	magnetosheath
NASA	National Aeronautics and Space Administration
SLAMS	short large amplitude magnetic structure(s)
SW	solar wind
SZA	solar zenith angle
THEMIS	Time History of Events and Macroscale Interactions during Substorms spacecraft
ULF	ultra-low frequency

Introduction

The interplanetary space is filled with charged particles originating from the Sun and cosmic ray sources outside of our solar system (Crosby, 2007). A constant flow of electrons and positive ions from the Sun makes up the *solar wind* (Parker, 1958). During its propagation, this plasma also drags out the Sun's magnetic field, forming the *interplanetary magnetic field* (IMF). On top of the solar wind that in itself varies in composition and speed, the Sun exhibits many types of events that release high-energy particles and clouds of plasma and magnetic fields into space. These so-called *space weather* events can be very harmful for our modern infrastructure consisting of technological systems on ground and in space, and for life (Bothmer and Daglis, 2007).

Fortunately, the Earth is protected by its magnetic field which prevents most charged particles from getting to the surface of the Earth. However, variations in the solar wind and the IMF can weaken this shield (Bothmer and Zhukov, 2007). Moreover, the Earth's magnetic field also has adverse effects as it guides charged particles down the magnetic field lines towards the Earth's polar regions and traps charged particles into the *magnetosphere*, the area under the influence of the Earth's magnetic field, holding them in *radiation belts* around the Earth (Crosby, 2007). As our presence in the near-Earth space and beyond increases, our satellites and astronauts need to be protected from these hazards, along with the modern technology and infrastructure on ground that we take for granted. Space physics is the field that studies this complex environment of the Earth's magnetosphere and its coupling with the solar wind, as a part of the near-Earth space environment.

In this thesis, we look into the interaction of the solar wind with the Earth's magnetosphere and study the region called the *magnetosheath*, where the solar wind flows around the magnetosphere. The basic structure of the system is illustrated in Figure 1. The solar wind is supersonic which leads to the formation of a *bow shock* in front of the Earth, just like in front of a supersonic jet flying through

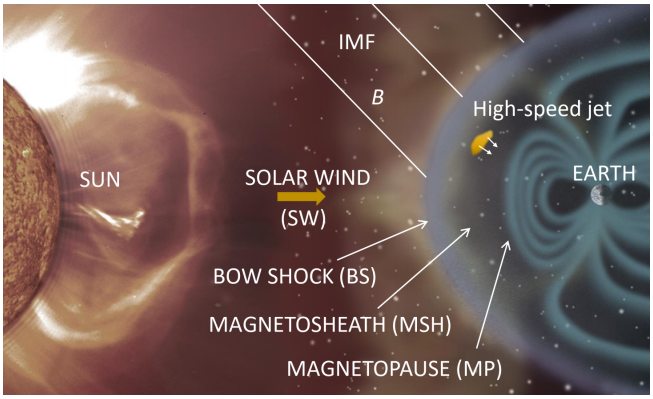

Figure 1. The Earth's magnetosphere in a meridian plane, where up is north and down is south. The solar wind flows out from the Sun into the interplanetary space, carrying its magnetic field with it forming the interplanetary magnetic field (IMF). The Earth's magnetic field stands as an obstacle to this supersonic flow, such that a bow shock is formed. The shocked solar wind flows around the Earth in the magnetosheath, between the bow shock and the magnetopause, where jets with higher earthward velocities are often observed. The image is not to scale. The background image credit: SOHO (ESA & NASA).

the air. The shock compresses and slows down the solar wind which can then flow around the Earth's magnetosphere in the magnetosheath, between the bow shock and the outer boundary of the magnetosphere, the *magnetopause*. Within the magnetosheath, plasma regions comparable to the size of the Earth with significantly higher earthward velocities than the background flow are often observed (Plaschke et al., 2018, and the references therein). These plasma structures have been named *magnetosheath jets*. The first observations of such structures were made over 20 years ago by Němeček et al. (1998), but during the last couple of years, these jets have been associated with multiple types of phenomena affecting the Earth's magnetosphere, which has led to a growing interest in these structures. These phenomena include, e.g., auroral brightenings (Wang et al., 2018) and the excitation of standing waves on the magnetopause (Archer et al., 2019). Following these observations, understanding where and when magnetosheath jets occur has become increasingly more important.

The IMF conditions greatly affect the dynamics of the Earth's magnetosphere (Eastwood et al., 2015, and the references therein). The IMF orientation affects the structure of the bow shock, which is believed to be closely linked to the formation

of magnetosheath jets (Hietala et al., 2009; Hietala and Plaschke, 2013; Karlsson et al., 2015), and it also determines the underlying magnetic field patterns in the magnetosheath (Fairfield, 1967). As the Earth's magnetic field points northward on its side of the subsolar magnetopause, a process called *magnetic reconnection* is driven when the magnetic field on the magnetosheath side points in the opposite direction — southward (Cassak and Fuselier, 2016, and the references therein). This process is naturally more prevalent during intervals of southward IMF. Magnetic reconnection connects the IMF and the Earth's magnetic field and it is a key process in transporting solar wind mass and energy into the magnetosphere (Cassak and Fuselier, 2016). Therefore, it is of great interest to study the magnetic field within magnetosheath jets because if it differs from the surrounding magnetic field, a jet could proposedly trigger or suppress this process when impacting the magnetopause (Hietala et al., 2018). Evidence of an event where a jet triggered magnetic reconnection has in fact already been provided by Hietala et al. (2018). However, in the event they studied, the magnetopause was too thick for reconnection to occur and it was the high dynamic pressure of the jet that caused the magnetopause to be compressed and ultimately led to reconnection. Additionally, in the case study of Nykyri et al. (2019), jets were suggested to have triggered magnetopause reconnection which then led to observed reconnection in the tail of the magnetosphere. In this event, which occured during northward IMF conditions, intervals of southward magnetic field within the magnetosheath were associated with jets.

In this thesis, we statistically study the magnetic characteristics of magnetosheath jets using 2008–2011 Time History of Events and Macroscale Interactions during Substorms (THEMIS) spacecraft data (Angelopoulos, 2008) from the magnetosheath and OMNI multi-spacecraft solar wind data (King and Papitashvili, 2005). We investigate how the IMF orientation controls where and how often these jets occur. We study their impact rates on the subsolar magnetopause as they are directly related to the prevalence of jet-induced effects in the magnetosphere. We note that this aforementioned study and its results have already been published by Vuorinen

et al. (2019). As jets have been linked to magnetopause reconnection events, we study the magnetic properties of jets themselves to better understand the role jets may have in affecting this key process in the magnetospheric dynamics.

We find that the IMF controls jet occurrence with jets occurring 9 times as often downstream of the quasi-parallel bow shock, where the IMF is almost parallel to the local shock normal, in comparison to the quasi-perpendicular region, where the IMF is almost perpendicular to the normal. Jets larger than 1 Earth radius in diameter are estimated to hit the subsolar magnetopause around 5–60 times per hour depending on the IMF orientation. Our results on the jets' magnetic fields close to to the magnetopause indicate that jets do not have statistical effect on magnetopause reconnection during southward IMF. However, we find that the magnetic field inside jets is favorable for enhancing the occurrence of magnetopause reconnection during northward IMF when the occurrence of reconnection would otherwise be low.

This thesis is organized as follows. We describe the background of the topics in Chapter 1. In Chapter 2, we describe the data and methods that were used in this study. In Chapter 3, we present the results and discuss them in Chapter 4. We summarize the results and give the conclusions in Chapter 5. In the end, in Chapter 6, we provide a brief outlook on possible future studies on the topic.

1 Background

In this chapter, we briefly describe the Earth's space environment, starting from the solar wind and the interplanetary magnetic field in Section 1.1. We use the solar wind data set of our statistical study (described in detail in Section 2.1) to provide supporting examples. Then we move on to the structure of the Earth's magnetosphere and aim to understand its dynamics in relation to the solar wind and IMF conditions in Section 1.2. As the dynamics of the bow shock are believed to be in a key role in jet generation (Plaschke et al., 2018, and the references therein), we give a compact explanation of collisionless shocks in space in order to understand the proposed formation mechanisms of magnetosheath jets. In Section 1.3, we also

describe the process of magnetic reconnection at the subsolar magnetopause. Lastly, in Section 1.5, we delve into the topic of magnetosheath jets — their occurrence, properties, and impacts on the magnetosphere.

1.1 The solar wind and the interplanetary magnetic field

The solar wind is a continuous flow of charged particles from the Sun that fills the whole solar system (Parker, 1958). This plasma originates from the hot outermost part of the solar atmosphere, the *corona*. Observationally, the solar wind is supersonic and it can be divided into two categories (Kallenrode, 1998, and the references therein): *fast* and *slow* solar wind. At around 1 AU (149,597,871 km, the astronomical unit) distance from the Sun where the Earth is located, the fast solar wind typically exhibits velocities in the range of 400–800 km/s and densities typically around 3 ions/cm^3. It originates from the Sun's coronal holes where the magnetic field lines are open, that is, one of their ends extends to space. Here, the solar wind is able to escape the Sun along the field lines without much resistance. Fast solar wind is generally stable with not much variation. Slow solar wind has velocities in the range 250–400 km/s and densities around 8 ions/cm^3 at 1 AU. It comes from regions of closed magnetic field lines: the edges of the coronal holes or from the streamer belt region near the solar equator during solar minima. It is much more variable in nature, and during a solar maximum the slow solar wind is observed to originate from a wide range of latitudes (Hansteen, 2009). In the data set used in this thesis, which consists of solar wind data from the years 2008–2011, the medians of the solar wind speed and density were 360 km/s and 6.8 ions/cm^3, respectively, but there is a lot of variation in both quantities. The year 2008 marked the start of a new solar cycle (NOAA: Space Weather Prediction Center, 2019). It started with a solar minimum and the solar activity began to rise significantly during the year 2011. Thus, most of our measurements were taken during the solar minimum, which explains why the solar wind was of the slow type.

The solar wind drags the Sun's magnetic field with it, forming the interplanetary

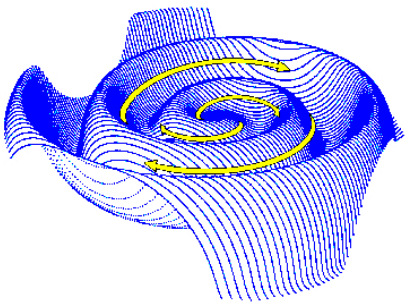

Figure 2. The interplanetary magnetic field (the yellow arrows) and the heliospheric current sheet (blue) around the Sun, which is in the center. Credit: J. Jokipii, University of Arizona (Heliophysics Science Division at NASA's GSFC, 2012).

magnetic field (Parker, 1958). The magnetic field is said to be *frozen into* the solar wind. This means that the magnetic field follows the plasma motion, i.e., it convects (advects, to be exact) with the solar wind (Kallenrode, 1998). This frozen-in condition is usually fulfilled in space plasmas due to their high conductivity which causes convection of the magnetic field to dominate over its diffusion (Koskinen, 2011). Therefore, as the Sun rotates around its axis, the ends of magnetic field lines frozen-in at the solar surface are dragged along with the rotation and the ends frozen into the radially out-flowing solar wind are dragged outward from the Sun. This results in the so-called *Parker spiral* pattern of the IMF, illustrated as the yellow arrows in Figure 2. The slower the solar wind speed, the tighter the spiral is wound into. On average, this Parker spiral makes a $\sim 45^\circ$ angle with the Sun-Earth line at 1 AU, where the Earth is located. This was also the most common value for the spiral angle in our data set. However, this a low-order approximation, as the IMF orientation is greatly affected by different solar wind structures and thus it keeps varying also at 1 AU (Koskinen, 2011). The magnitude of the IMF is in the nanotesla range and in our data set its median was 4.3 nT, which represents typical IMF conditions (Eastwood et al., 2015).

The polarity or the direction of the IMF, whether the field points earthward or sunward, also varies following the polarity of the Sun's magnetic field (Kallenrode, 1998). The neutral line on the Sun between the different polarities, inward and

outward, is not aligned with the equator of the Sun but instead keeps crossing it. As the field is dragged out from the Sun, the *heliospheric current sheet* (HCS) (shown in blue in Figure 2) is formed between the northward and southward magnetic field regions of different polarities, obeying the Ampère's law:

$$\nabla \times \mathbf{B} = \mu_0 \mathbf{J}, \tag{1}$$

where $\mathbf{B}$ is the magnetic field, μ_0 is the permeability of vacuum and $\mathbf{J}$ is the current density. The HCS has an undulating structure due to the inclinations of the neutral line combined with the Parker spiral. As the Earth moves through space, it keeps crossing the wavy HCS and the polarity of the IMF at Earth varies. In our data set, the IMF vector component parallel to the Sun-Earth line was sunward 60 % of the time and, conversely, anti-sunward 40 % of the time.

The solar wind also exhibits waves, turbulence and many types of transient events and structures (Kallenrode, 1998). Several types of discontinuities, such as shock waves (described in Section 1.2), can also form within the solar wind. Importantly, these disturbances and structures also cause variations in the IMF due to the frozen-in condition. For example, *co-rotating interaction regions* (CIRs) and *coronal mass ejections* (CMEs) are two common large-scale structures in the solar wind. CIRs form between streams of slow and fast solar wind as the fast solar wind catches up with the slow solar wind causing the plasma and the spiral magnetic field lines to pile up (Koskinen, 2011). CMEs, on the other hand, are large magnetized plasma structures released from the corona (Kallenrode, 1998). Many CMEs are fast enough to drive shock waves ahead of them while propagating in the solar wind. Since the Earth's magnetosphere (described in Section 1.2) is small compared to the size scale of these transients and to spatial IMF fluctuations in general, the solar wind and IMF conditions can be approximated to be homogeneous but time-variant around Earth. In this study, we assume the solar wind conditions across the whole subsolar bow shock region to be uniform.

1.2 Structure and dynamics of the Earth's magnetosphere

As mentioned in Section 1.1, the solar wind is supersonic and shock waves can form within the solar wind. This is analogous to a shock forming in front of a supersonic aircraft. In everyday fluids, gases and liquids, the sound speed is the speed of mechanical waves or disturbances in the medium (Kallenrode, 1998). Sound waves cannot bring information about an approaching supersonic aircraft before the arrival of the aircraft itself (Burgess and Scholer, 2015). Therefore, the air in front of the aircraft cannot deflect and the aircraft catches the sound waves which ultimately steepen into a shock wave. The shock wave transforms kinetic energy of the flow into thermal energy, and thus slows down the flow and abruptly increases the temperature and the sound speed of the medium (Kallenrode, 1998). As a result, the shock transforms the upstream supersonic flow into a subsonic downstream flow which can then divert around the aircraft.

The same process can occur in plasmas, e.g., the solar wind, that are ionized fluids in which electric and magnetic fields are important for the dynamics (Koskinen, 2011). Plasma shocks are in fact ubiquitous in the universe and they are important acceleration sites of charged particles (Balogh et al., 2005). The closest one to us is the bow shock formed in front of the Earth's magnetosphere. In this case, the Earth's magnetic field acts as an obstacle to the supersonic solar wind. While particle collisions play an important role in gas-dynamical shocks by causing the dissipation of kinetic energy into thermal energy, collisions are rare in the low-density solar wind plasma (Kallenrode, 1998). In such *collisionless plasma shocks*, the dissipation is caused by the interaction of the particles and the magnetic field (Kallenrode, 1998). In plasmas, there are also additional speeds for the propagation of disturbances: the Alfvén speed and the fast and slow magnetosonic speeds (Burgess and Scholer, 2015). Since the solar wind is also super-Alfvénic and super-fast-magnetosonic, the Earth's bow shock is a so-called *fast-mode shock*, like most astrophysical shocks (Burgess and Scholer, 2015). A fast-mode shock is characterized by an increase of

the magnetic field magnitude across the shock. In our data set (described in Section 2.1), the median magnetic field magnitude in the subsolar magnetosheath was 26 nT and the median IMF magnitude was 4.3 nT.

The theory of *magnetohydrodynamics* (MHD) allows us to calculate how the macroscopic properties of plasma change across a shock (Koskinen, 2011). MHD treats plasma as a magnetized fluid and combines the equations of hydrodynamics and electromagnetism. Ideal MHD, which makes simplifying assumptions of the Ohm's law, e.g., that of infinite conductivity, provides us with the *Rankine-Hugoniot jump conditions* that describe how the macroscopic properties of plasma change in dynamic equilibrium over an infinitely thin but infinitely wide planar discontinuity between two homogeneous plasma regions (upstream and downstream):

$$[\rho V_n] = 0 \tag{2}$$

$$\left[\rho \mathbf{V} V_n + \left(P + \frac{B^2}{2\mu_0}\right)\hat{\mathbf{n}} - \frac{B_n \mathbf{B}}{\mu_0}\right] = 0 \tag{3}$$

$$\left[\left(\frac{1}{2}\rho V^2 + \frac{\gamma P}{\gamma - 1} + \frac{B^2}{\mu_0}\right) V_n - \frac{B_n \mathbf{B}\cdot\mathbf{V}}{\mu_0}\right] = 0 \tag{4}$$

$$[\mathbf{B}_n] = 0 \tag{5}$$

$$[V_n \mathbf{B}_t - B_n \mathbf{V}_t] = 0. \tag{6}$$

The notation $[a] = a_2 - a_1$ refers to the change of quantity a across the discontinuity, from the upstream value a_1 to the downstream value a_2. $\mathbf{V}$ is the bulk flow velocity, $\mathbf{B}$ is the magnetic field, P is the plasma pressure, ρ is the mass density, μ_0 is the vacuum permeability, and γ is the polytropic index. The vector components parallel to the discontinuity normal $\hat{\mathbf{n}}$ are denoted with the subscript n and the components tangential to the discontinuity are denoted with the subscript t. The jump conditions are based on the conservation of mass, momentum, and energy (Eqs. (2)–(4)). The last two conditions (Eq. (5)–(6)) are based on two of the Maxwell's equations:

$$\nabla \cdot \mathbf{B} = 0 \tag{7}$$

$$\nabla \times \mathbf{E} = 0, \tag{8}$$

Gauss' law for magnetism and Faraday's law in the steady state, respectively.

The Rankine-Hugoniot relations can be used to model multiple types of discontinuities, shocks being one of them. Shocks are solutions where there is mass flow $V_n > 0$ across the discontinuity. Across a shock, V_n decreases and ρ increases (Burgess and Scholer, 2015). The angles that the shock normal makes with the upstream bulk velocity and with the upstream magnetic field determine the shock geometry and the dynamics of the shock (Burgess and Scholer, 2015). The angle between the flow and the shock normal largely determines how much the total flow velocity is slowed down and compressed because the deceleration is the most efficient for the V_n component. This is why shocks are commonly characterized by their *Alfvén Mach number* $M_\mathrm{A} = V_{1n}/V_{1\mathrm{n,A}}$, the ratio between the upstream normal bulk velocity component and the upstream characteristic Alfvén wave speed $V_{1\mathrm{n,A}} = B_{1n}/\sqrt{\mu_0\rho_1}$. The Alfvén Mach number describes the strength of the shock.

The angle between the upstream shock normal and the upstream magnetic field is notated with θ_{Bn}. On top of its role in the MHD jump conditions, it is also very important for the kinetic structure of the shock. A shock region with $\theta_{Bn} < 45°$ is called a *quasi-parallel shock* and correspondingly a region with $\theta_{Bn} > 45°$ is a *quasi-perpendicular shock* (Balogh et al., 2005). Particles reflected from the shock cause the macroscale structures of quasi-parallel and quasi-perpendicular shock regions to be very different. At a quasi-perpendicular shock, particles reflecting from the shock get swiftly carried downstream by the flow as they cannot move perpendicular to the magnetic field (Burgess and Scholer, 2015). Hence, these particles do not have time to largely affect the macroscopical structure of the shock, and a quasi-perpendicular shock transition is sharp. In contrast, at quasi-parallel bow shock regions, where the IMF is nearly parallel to the local shock normal, some of the solar wind particles can gain enough energy during the shock transition to reflect and escape far upstream of the shock along these field lines (Burgess and Scholer, 2015). The escaping particles and their interaction with the in-flowing solar wind cause the quasi-parallel shock to be extended upstream into a turbulent *foreshock* region. The foreshock exhibits, e.g.,

field-aligned backstreaming particle distributions and ultra-low frequency (ULF) waves (Eastwood et al., 2005).

Observations (e.g., Schwartz and Burgess, 1991; Lucek et al., 2008) and simulations (e.g., Blanco-Cano et al., 2009, 2011) have shown that foreshock processes cause the quasi-parallel shock itself to be structured and corrugated. Schwartz and Burgess (1991) suggested that the structure of the quasi-parallel shock could be explained with *short large amplitude magnetic structures* (SLAMS) that merge into the shock. SLAMS are around 10-second pulsations of enhanced magnetic field observed advecting toward the bow shock in the foreshock region (Schwartz, 1991). They are formed from steepened ULF waves (Giacalone et al., 1993). In this picture, the quasi-parallel shock consists of a patchwork of SLAMS (Schwartz and Burgess, 1991), and this uneven structure causes the observed rippling of the shock surface. This theory has gained supporting observational evidence, e.g., by Lucek et al. (2008).

The global position of the bow shock varies as the dynamic pressure of the solar wind compresses the magnetosphere (e.g., Formisano, 1979; Merka et al., 2005). A typical stand-off distance of the bow shock on the Sun-Earth line is around $13\,R_{\mathrm{E}}$ ($R_{\mathrm{E}} = 6{,}371\,\mathrm{km}$, the Earth's radius) from the center of the Earth (Koskinen, 2011). The shape of the bow shock is determined by the shape of the obstacle (Burgess and Scholer, 2015), so the Earth's bow shock is approximately shaped like a paraboloid around the Sun-Earth line due to the form of the dayside magnetopause that encloses the Earth's magnetic field. This is illustrated in a 2D cross-section in Figure 1. Due to the curvature of the bow shock, the direction of the shock normal vector varies greatly along the shock and the local shock dynamics change with different parts of the bow shock being quasi-parallel and quasi-perpendicular even during a constant IMF orientation (Burgess and Scholer, 2015). Furthermore, as the IMF orientation varies with time due to changes in solar wind conditions, the local shock dynamics change. In Figure 3, we can see illustrations of the locations of the foreshock and the quasi-parallel and quasi-perpendicular bow shock regions during three different

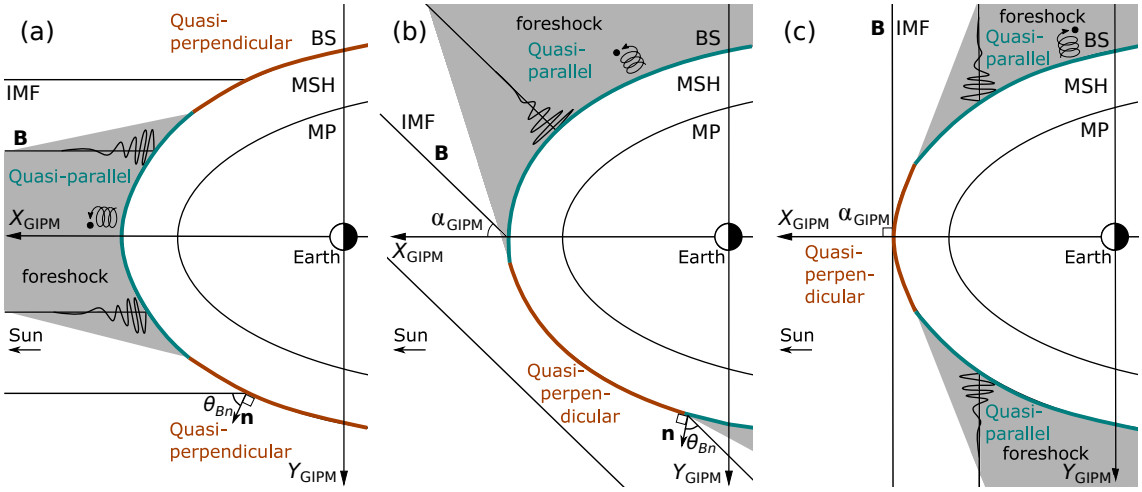

Figure 3. A sketched figure of the approximate locations of the foreshock region (gray) and the quasi-perpendicular (brown) and quasi-parallel (turquoise) regions of the bow shock (BS) for three different IMF orientations with IMF cone angles: (a) $\alpha_{\mathrm{GIPM}} \sim 0°$, (b) $\alpha_{\mathrm{GIPM}} \sim 45°$, and (c) $\alpha_{\mathrm{GIPM}} \sim 90°$. The figures are presented in the plane containing the IMF and with the X_{GIPM}-axis anti-parallel to the solar wind velocity. The GIPM frame is described in Section 2.2. The figure is adapted from Vuorinen et al. (2019) and licensed under CC BY.

IMF orientations. During radial IMF (Figure 3a), the subsolar magnetosheath is downstream of the quasi-parallel shock. As the obliquity of the IMF increases, one side of the bow shock becomes quasi-parallel and the other becomes quasi-perpendicular (Figure 3b) and, finally, the subsolar magnetosheath is downstream of the quasi-perpendicular shock (Figure 3c).

Once the solar wind has been slowed down, compressed, and deflected by the bow shock, it can flow around the magnetosphere in the magnetosheath. Fairfield (1967) demonstrated using IMP 1 and IMP 2 (Interplanetary Monitoring Platform) satellite data that the IMF is convected into the magnetosheath along with the shocked solar wind. According to the results, the IMF conditions largely determine the properties of the magnetic field within the magnetosheath and IMF discontinuities can be later observed in the magnetosheath as well. Despite the magnetosheath being a turbulent plasma region filled with fluctuations, the results showed that its magnetic field is actually more ordered than the IMF. This had been previously predicted by the hydromagnetic flow models of, e.g., Spreiter et al. (1966): the field lines are

draped around the magnetosphere with the tendency of becoming tangential to the magnetopause.

The magnetopause separates the magnetospheric plasma and the magnetosheath plasma, and their respective magnetic fields, following the frozen-in condition of high conductivity space plasmas (described in Section 1.1). A low-order estimation of its location can be determined by the pressure balance between the magnetic pressure of the magnetosphere and the dynamic pressure of the solar wind (Kallenrode, 1998). A typical subsolar stand-off distance of the magnetopause is around $10\,R_{\mathrm{E}}$ from the center of the Earth. The Earth's magnetic field deflects the incoming charged magnetosheath particles by the magnetic Lorentz force:

$$\mathbf{F} = q\mathbf{v} \times \mathbf{B}, \tag{9}$$

where q is the charge of the particle, $\mathbf{v}$ is its velocity, and $\mathbf{B}$ is the Earth's magnetic field in this case. As positive and negative charges are deflected in opposite directions, currents are produced. The magnetopause is in fact a current layer wrapped around the Earth's magnetic field. On the nightside of the magnetosphere, the solar wind pulls the magnetosphere outward, forming a tail region that extends to over a hundred Earth radii (Kallenrode, 1998). However, between the closed dayside field lines and those open nightside field lines that are dragged to the tail, there are two special regions, the southern and northern *polar cusps*, where the magnetic fields are weak and particles can freely stream into the polar regions (Kallenrode, 1998).

1.3 Magnetic reconnection at the subsolar magnetopause

The dayside magnetopause is not a perfect boundary, either. The magnetosheath magnetic field and the Earth's magnetic field can reconnect to each other, allowing magnetosheath plasma and magnetospheric plasma to mix. This process of magnetic reconnection is a fundamental process in plasma physics, ubiquitous in plasmas all around the universe (Yamada et al., 2010): it is the process that releases high-energy particles and magnetic clouds from the surface of the Sun, allows the transfer

of solar wind mass and energy into the magnetosphere, and also occurs in fusion reactors. Magnetic reconnection at the magnetopause and in the tail of the Earth's magnetosphere plays a very significant role in space weather events.

As explained for the heliospheric current sheet (Section 1.1) and the magnetopause (Section 1.2), a local magnetic field gradient between two plasma populations leads to a formation of a current sheet between these two regions following the Ampère's law (Eq. (1)) (Koskinen, 2011). In thin current sheets, the current density can become high enough for the resistivity increase so that the frozen-in condition is ultimately broken down and the plasma loses control of the magnetic field (Koskinen, 2011). This allows for the diffusion of the magnetic field to take place. In magnetic reconnection, the field gradients are large and the diffusion happens abruptly. Such large gradients are usually obtained by large magnetic shear, meaning that the angle between the magnetic field vectors on the opposite sides of the interface is large. Thus, magnetic reconnection tends to occur where the magnetic fields of the two populations are almost anti-parallel (Cassak and Fuselier, 2016). Reconnection arranges the magnetic topology by minimizing magnetic energy (Yamada et al., 2010). This happens on the *X-line* or the neutral line between the two plasmas, where the magnetic field magnitude becomes very small due to the cancellation between the fields of the two populations. The magnetic energy released during this process is transformed into thermal and kinetic energy of the plasma.

In magnetopause reconnection, the magnetosheath magnetic field and the magnetospheric field connect to each other and the plasmas of these two regions are mixed (Cassak and Fuselier, 2016). On the Earth's side of the magnetopause, the magnetospheric magnetic field does not exhibit large variations. The field is typically around 50–60 nT and points northward close to the subsolar magnetopause (Cassak and Fuselier, 2016). Therefore, the magnetic field conditions on the magnetosheath side, affected by the upstream solar wind conditions, largely determine the occurrence of magnetopause reconnection. This is illustrated in Figure 4. Reconnection

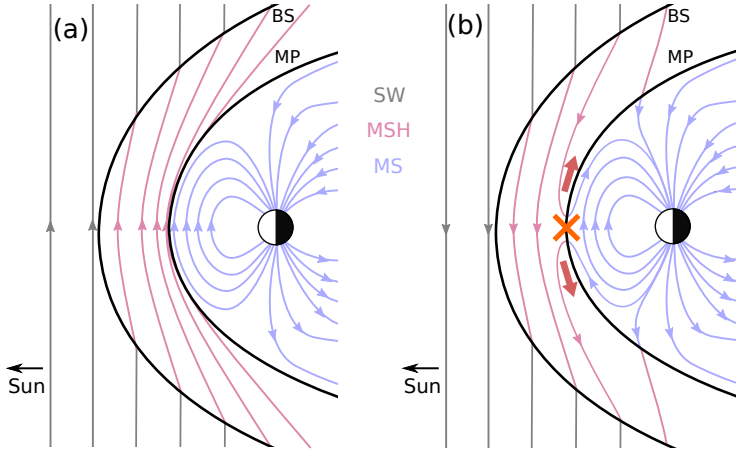

Figure 4. Sketches illustrating the magnetic field configuration in the solar wind (SW), magnetosheath (MSH), and the magnetosphere (MS) during (a) northward and (b) southward IMF in the meridian plane where north points upward. During northward IMF, the occurrence of dayside magnetopause reconnection is low and the magnetic field piles up in front of the magnetopause. During southward IMF, dayside magnetopause reconnection is very common. The orange cross is the X-line, extending in and out of the page, where the magnetic field becomes very weak and the reconnection of the field takes place. The red arrows represent plasma flows accelerated by the reconnection.

at the subsolar magnetopause is not that common during northward IMF when the magnetic shear is low (Cassak and Fuselier, 2016). This leads to the accumulation of magnetic flux in front of the magnetopause and the formation of the so-called *magnetic pile-up layer* (Phan et al., 1994). Due to the increase of magnetic pressure, plasma density has to decrease in order to maintain pressure balance. Therefore, plasma is squeezed away along the field lines. This layer of magnetic pile-up and decrease of plasma density is also called the *plasma depletion layer* (Phan et al., 1994). In contrast, when the IMF is aligned southward, the magnetic shear is high and reconnection at the subsolar magnetopause is driven efficiently (Cassak and Fuselier, 2016) with magnetic field energy being constantly released at the dayside magnetopause (Phan et al., 1994). In Figure 4b, we can also see an illustration of how the field lines reconnect at the X-line and the plasma flows away from the reconnection site. The solar wind then drags these newly opened field lines to the tail of the magnetosphere. Magnetic reconnection allows for the magnetosheath plasma to enter the magnetosphere along these reconnected field lines.

1.4 Magnetospheric coordinate systems

When studying magnetic fields in the magnetosphere, the *Geocentric Solar Magnetospheric coordinate system* (GSM) is commonly used (e.g., Eastwood et al., 2015). In this frame, the X_{GSM}-axis is along the Sun-Earth line pointing sunward. The X_{GSM}–Z_{GSM}-plane contains the Earth's magnetic dipole axis with the direction of positive Z_{GSM} corresponding to the north pole of the magnetic dipole. The Y_{GSM}-axis completes the coordinate system in the right-handed sense. In this frame, a northward magnetic field has $B_{Z,\mathrm{GSM}} > 0$ and a southward magnetic field has $B_{Z,\mathrm{GSM}} < 0$.

Another widely used frame is the *Geocentric Solar Ecliptic coordinate system* (GSE) (e.g., Hapgood, 1992). The X_{GSE}-axis is equivalent to the X_{GSM}-axis. The other two axes are defined as follows: the X_{GSE}–Y_{GSE} plane spans the ecliptic plane, i.e., the Earth's plane of orbit around the Sun, with the Y_{GSE}-axis pointing against the Earth's orbital velocity. The Z_{GSE}-axis completes the coordinate system by pointing northward perpendicular to the ecliptic plane.

1.5 Magnetosheath jets

Just like many types of transient structures are observed in the solar wind, there are different kinds of plasma entities present in the magnetosheath flow. In this thesis, we will focus on magnetosheath jets that are localized enhancements of dynamic pressure:

$$P_{\mathrm{dyn}} = \rho V^2. \tag{10}$$

These structures are interesting because, due to their high dynamic pressure, they can have significant effects on the magnetosphere and the *ionosphere* (the ionized layer of the Earth's upper atmosphere) when interacting with the magnetopause (Plaschke et al., 2013). A comprehensive review of magnetosheath jets was recently published by Plaschke et al. (2018). We will be using this review as a guiding reference in this section but also cover new results that have been reported after this review was published.

1.5.1 History

The study of magnetosheath jets or similar structures started over 20 years ago when observations of transient ion flux (ρV) enhancements in the magnetosheath were first published by Němeček et al. (1998). Since then, these phenomena have gained increasing popularity among space physicists, and what started as case studies (e.g., Němeček et al., 1998, 2000; Hietala et al., 2009; Archer et al., 2012) has led to large statistical studies (e.g., Archer and Horbury, 2013; Plaschke et al., 2013; Gutynska et al., 2015). Ultimately, it has been found that the magnetosheath exhibits many types of enhancements of dynamic pressure, density, velocity, or flux with different types of properties and origins (see Plaschke et al. (2018) for a review). During the last couple of years, case studies have linked magnetosheath jets to various magnetospheric phenomena such as particular type of auroras (Wang et al., 2018), triggering of magnetopause magnetic reconnection (Hietala et al., 2018; Nykyri et al., 2019), and just recently, excitation of magnetopause standing waves (Archer et al., 2019). There are still many open questions regarding these transient structures, namely how they are formed and what is their importance in the solar wind-magnetosphere interaction. These topics are actively studied and, e.g., there is a lot of effort put into the development of simulations of the bow shock where the jets are expected to be formed. Jet-like structures have already been observed in many 2D simulations (e.g., Hao et al., 2016; Palmroth et al., 2018) and currently, the first 3D simulations of representable size are being developed.

1.5.2 Definitions

As reviewed by Plaschke et al. (2018), many different names and definitions have been used for dynamic pressure enhancements in the magnetosheath (Savin et al., 2008; Amata et al., 2011; Hietala et al., 2012; Archer et al., 2012; Archer and Horbury, 2013; Savin et al., 2014). Similar types of magnetosheath transients have also been studied with thresholds imposed on other quantities such as flux (Němeček et al., 1998), density (Karlsson et al., 2012, 2015; Gutynska et al., 2015), earthward

velocity (Hietala et al., 2012; Gunell et al., 2014), and total pressure (Dmitriev and Suvorova, 2015). As shown by Plaschke et al. (2018), these different definitions exhibit partly overlapping selections of events and partly different properties.

In this thesis, we will be using the definition of magnetosheath jets given by Plaschke et al. (2013) for the study of the subsolar magnetosheath. They studied the subsolar magnetosheath using 2,736.9 hours of data from the Time History of Events and Macroscale Interactions during Substorms (THEMIS) spacecraft from the years 2008–2011. They defined jets such that the earthward ion dynamic pressure within a jet has to exceed half of the solar wind total ion dynamic pressure, that was averaged over the preceding five minutes. I.e., in the GSE frame:

$$P_{\mathrm{dyn,MSH},X} = \rho_{\mathrm{MSH}} V_{\mathrm{MSH},X}^2 > \frac{1}{2} P_{\mathrm{dyn,SW}} = \frac{1}{2} \rho_{\mathrm{SW}} V_{\mathrm{SW}}^2. \tag{11}$$

They defined jets specifically as enhancements of earthward dynamic pressure because these jets are the most likely ones to impact the magnetopause and cause processes that affect the Earth. Furthermore, the threshold is based on the dynamic pressure of the solar wind to make sure that these transients are not just solar wind discontinuities, but structures that are actually formed at some point when the solar wind interacts with the foreshock-bow shock system and flows within the magnetosheath.

In Figure 5, we have spacecraft measurements where we can see an example of such a jet event. In the bottom panel (e), we can see a time series of dynamic pressure in the magnetosheath (the black line). The dynamic pressure exceeds half of the solar wind dynamic pressure (the blue line). The moment of highest dynamic pressure is notated with t_0 and the whole jet interval is defined as the interval when the dynamic pressure is over 1/4 of the total solar wind dynamic pressure (the green line). The criteria of Plaschke et al. (2013) also require that within the one-minute long intervals before and after the jet, called pre-jet and post-jet intervals, the ion velocity in the X_{GSE}-direction (the blue line in panel (b)) has to exceed half of that value at t_0 (the dash-dotted horizontal line). This ensures that jets are truly localized

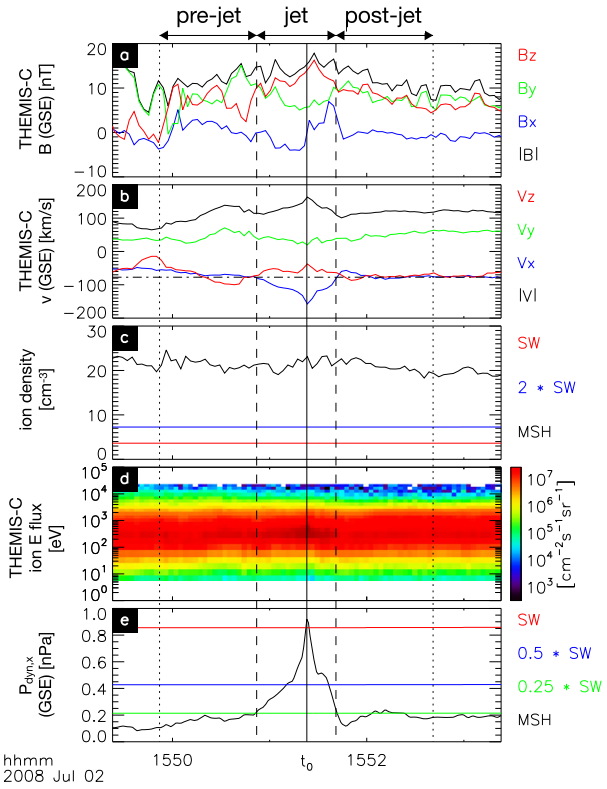

Figure 5. THEMIS C time series data of an example magnetosheath jet illustrating the jet selection criteria. The figure is from Plaschke et al. (2013) and licensed under CC BY.

entities and consecutive peaks are not counted as individual jets. Ultimately they obtained a set of 2,859 observed jets.

In addition to the results of Plaschke et al. (2013), we will also be discussing the results of another large statistical study of dynamic pressure enhancements published by Archer and Horbury (2013). They used THEMIS data from 2008 totaling 1,361 hours of dayside magnetosheath data. The selection criteria applied by them differ from those of Plaschke et al. (2013). Archer and Horbury (2013) used the background magnetosheath dynamic pressure as their threshold value for dynamic pressure enhancements, defining them as magnetosheath plasma regions with larger than a 100 % increase in total ion dynamic pressure compared to a 20-minute running average. Using these criteria, they obtained 2,617 dynamic pressure enhancements. According to the comparison made by Plaschke et al. (2018), in which they applied the Plaschke et al. (2013) criteria to the data set used by Archer and

Horbury (2013), 83 % of the enhancements found by Archer and Horbury (2013) were not magnetosheath jets on the standards of Plaschke et al. (2013). Conversely, 53 % of jets identified with Plaschke et al. (2013) criteria were not dynamic pressure enhancements defined by Archer and Horbury (2013). This shows that different definitions produce significantly different data sets. Therefore, results obtained for one definition cannot be directly applied to another without investigation.

1.5.3 Occurrence

Plaschke et al. (2013) found that jets are observed more often closer to the bow shock than to the magnetopause (Figure 6a) and their occurrence is strongly controlled by only one parameter: the orientation of the interplanetary magnetic field (IMF). More precisely, they reported that in the subsolar magnetosheath, jets mostly occur during low IMF cone angle conditions, that is, when the acute angle between the the Sun-Earth (the X_{GSE}-axis) and the IMF is small ($< 45°$) (Figure 6b). Low IMF cone angle conditions correspond to the subsolar magnetosheath being downstream of the quasi-parallel shock because the bow shock normal is almost parallel to the X_{GSE}-axis at the subsolar bow shock region. Thus, the IMF cone angle α_{GSE} can be used to estimate θ_{Bn}. Similar results relating these structures to the quasi-parallel shock had already been reported in case studies by, e.g., Němeček et al. (2000), Savin et al. (2008), and Hietala et al. (2009). This result also agrees with the conclusion of Archer and Horbury (2013) that dynamic pressure enhancements mostly occur with small θ_{Bn}, that is, downstream of the quasi-parallel bow shock. In a large statistical study of subsolar magnetosheath THEMIS data and 1,312 density enhancements, Gutynska et al. (2015) also reported the same dependence on low IMF cone angle and θ_{Bn}. These results indicate that the quasi-parallel shock and the foreshock region play important roles in jet generation and, in general, more transients are observed downstream of the quasi-parallel shock.

Archer and Horbury (2013) also found that the IMF tends to be steadier than usual during jet observations, suggesting that solar wind variations are not a primary

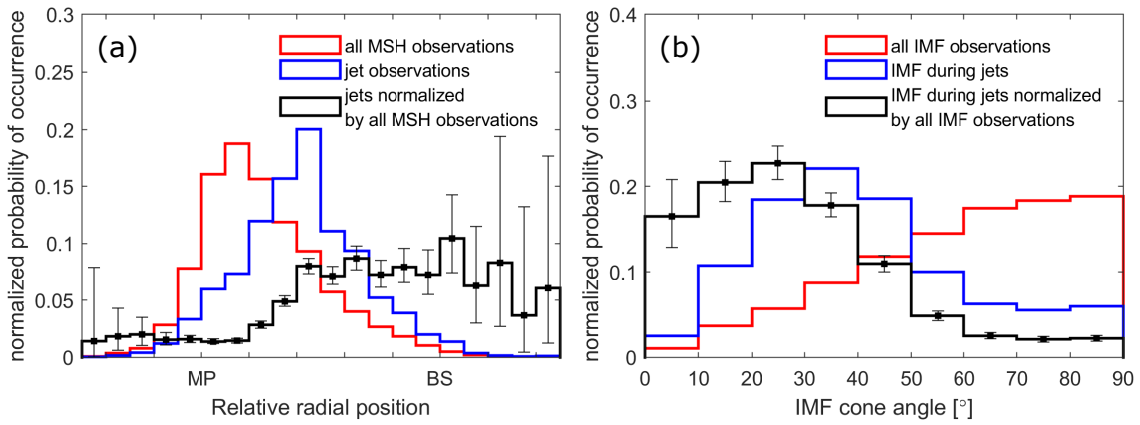

Figure 6. Plaschke et al. (2013) results on the distributions of (a) relative radial positions between the magnetopause and the bow shock and (b) GSE IMF cone angle conditions for all magnetosheath observations (red), jet observations at t_0 (blue) and jets normalized by all magnetosheath distributions (black). These figures are reproduced from Plaschke et al. (2013) (licensed under CC BY). We have included 95 % Clopper-Pearson binomial confidence intervals and used slightly different corrections for solar wind aberration in the model bow shocks and magnetopauses.

driver of jets. This result suggests that a stable foreshock region provides good conditions for jet formation. However, interestingly, Archer and Horbury (2013) did not observe increased occurrence rates closer to the bow shock, but actually closer to the magnetopause for those transients that were observed downstream of the quasi-perpendicular shock. This strongly indicates that the definition used by Archer and Horbury (2013) includes transients generated by different mechanisms.

According to the observational results provided by Plaschke et al. (2013) and backed by the simulation results of Hao et al. (2016), jets occur randomly without any preferred recurrence times. Using the data set of Plaschke et al. (2013), we calculate that the occurrence rate of jets in the subsolar magnetosheath is around 3 jets per hour (4 % of all magnetosheath observations made up by jet intervals) during the favorable low IMF cone angle conditions ($< 30°$). For high cone angles ($\geq 60°$), 0.3 jets occurred per hour (0.4 % of observations made up by jet intervals). In the Archer and Horbury (2013) study, the fractions made up by the dynamic pressure intervals in all dayside magnetosheath observations were 3 % downstream of the quasi-parallel shock and 0.5 % downstream of the quasi-perpendicular shock.

The first one increases to 10 % when only considering observations in the subsolar magnetosheath, defined by the aberrated solar zenith angle (SZA) $\theta_{\mathrm{SZA}} < 30°$ (the angle between an Earth-centered position vector and the Sun-Earth line). Therefore, their selection criteria seem to find more dynamic pressure enhancements than Plaschke et al. (2013).

Although magnetosheath jets have been extensively linked to the quasi-parallel shock, the spatial occurrence of jets has not yet been studied in detail. In this thesis, we aim to provide quantitative results on where jets occur during different IMF orientations.

1.5.4 Properties

For most, the term *jet* evokes an image of a very elongated bursty structure. However, in multi-spacecraft observations magnetosheath jets have been found to be plasma blobs with a typical scale size of around 1 R_{E} (Plaschke et al., 2018, and the references therein). While the scale size is somewhat agreed upon, different studies have given different results on the shape of jets. Plaschke et al. (2016) found jets to have larger size perpendicular to their flow direction than parallel to their flow direction (estimated median values of 0.93 R_{E} and 0.49 R_{E}, respectively) but Archer and Horbury (2013) found the opposite.

Plaschke et al. (2013) observed jets exhibiting dynamic pressure around 3–25 times the ambient background magnetosheath dynamic pressure, and Archer and Horbury (2013) observed dynamic pressure enhancements of 2–15 times the ambient value. While dynamic pressure is also a function of density, both studies reported most transients being dominated by the velocity increases. Archer and Horbury (2013) observed 82 % of their jets to have increase in both quantities, density and velocity. They could link the events observed close to the subsolar magnetopause to the events where density decreases and concluded that they were most likely *flux transfer events* (FTEs) associated with reconnection events at the magnetopause. FTEs are not included in the data sets of Plaschke et al. (2013) because they do

not exhibit high earthward velocities. Plaschke et al. (2013) reported 89.5 % of jets were associated with a density increase.

Both Plaschke et al. (2013) and Archer and Horbury (2013) observed that the velocities within the jets were usually super-Alfvénic and sometimes even higher than the local magnetosonic velocity in the subsolar region. Therefore, some jets should develop bow waves that can eventually steepen into shock fronts of their own. Observational evidence of a jet-driven bow wave was recently published by Liu et al. (2019). The propagation direction of jets also tends to deviate from the background flow, at least according to Plaschke et al. (2013) who reported a median of 28.6° and Hietala and Plaschke (2013) who reported a range of 20°–34°. Hietala and Plaschke (2013) concluded that jets exhibit velocities that are more aligned anti-parallel to the Sun-Earth line and as the jets move closer to the magnetopause, the deflection from the background flow grows. According to them, this suggests that while the background flow keeps diverting due to the approaching magnetopause, jets continue more or less along their original propagation direction.

The magnetic field magnitude inside jets can be larger or smaller than within the pre-jet magnetosheath plasma, with increases being slightly more common (Plaschke et al., 2013; Archer and Horbury, 2013). In addition, Karlsson et al. (2015) have studied magnetosheath density enhancements called *plasmoids* which usually exhibit a clear decrease or increase in magnetic field magnitude. Some of these plasmoids have higher velocities than the surrounding magnetosheath and these fast plamoids tend to exhibit increased magnetic field magnitudes. Besides the field magnitude, the magnetic field within jets has not been studied in detail. We will take a closer look at this important property, mainly focusing on the north-south component of the magnetic field because of its significance for magnetopause reconnection.

1.5.5 Possible formation mechanisms

As jets are observed more often closer to the bow shock than to the magnetopause and most jets are linked to the quasi-parallel shock, it seems reasonable to assume

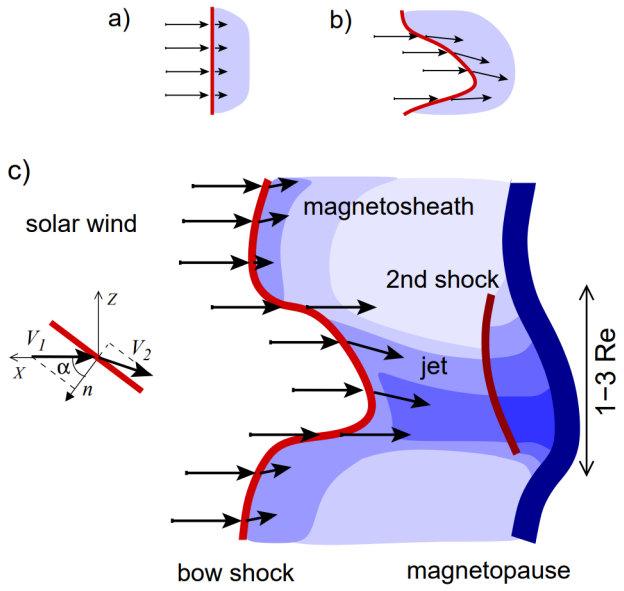

Figure 7. Bow shock ripples have been proposed to produce magnetosheath jets. Here the arrows at the bow shock denote flow velocity and the darker the blue in the magnetosheath, the higher the plasma density. (a) Flow that is parallel to the local shock normal is slowed down efficiently. (b) A rippled shock can produce faster moving regions of plasma. (c) The rippling of the bow shock could therefore produce jets. Shocks can also develop in the magnetosheath when the backstreaming flow from the magnetopause interacts with the high-speed jet. The figure is from Hietala et al. (2012) and licensed under CC BY.

that the formation of most jets is related to foreshock processes (Plaschke et al., 2018, and the references therein). Consequently, several jet formation mechanisms related to the nature of the turbulent foreshock region and the quasi-parallel shock have been suggested. Here we consider the two most promising ones: bow shock ripples and short large amplitude magnetic structures (SLAMS) that were both described in Section 1.2.

Hietala et al. (2009) proposed that local curvature variations of the bow shock, which are inherent to the quasi-parallel shock, could be responsible for jet generation. According to the Rankine-Hugoniot jump conditions described by Eqs. (2)–(6), a ripple in the shock surface can theoretically produce less decelerated flows of compressed solar wind plasma. This process is illustrated in Figure 7. Here we give a simplified explanation for the mechanism. See Hietala et al. (2009, 2012) and Hietala and Plaschke (2013) for more detailed explanations and derivations.

Assuming a high M_{A} shock, the tangential velocity component of the flow does not change much across the shock: $V_{2t} \approx V_{1t}$ (Hietala et al., 2012). However, the normal component of the flow changes according to Eq. (2): $V_{2n} = \rho_1 V_{1n}/\rho_2 = V_{1n}/r_{\mathrm{comp}}$ ($r_{\mathrm{comp}} > 1$ is the shock compression ratio). Therefore, as the acute angle α between the upstream plasma velocity and the local shock normal grows, the deceleration of the plasma flow at the shock decreases. This is illustrated in Figures 7a and 7b. Thus, a ripple geometry, such as the one shown in Figure 7c, could guide less decelerated plasma into a localized plasma region — a jet. Hietala and Plaschke (2013) studied the bow shock ripple mechanism and, according to their results, 97 % of their jet observations could be explained with this formation mechanism. They modelled the ripples as sinusoidal waves present 12 % of the time with the amplitude to wavelength ratio of around 0.1 R_{E} to 1.1 R_{E}. The amplitude corresponds quite well to observational estimations of SLAMS sizes by Lucek et al. (2008) and the wavelength was tuned to produce jets with transverse sizes of 0.5–1.0 R_{E}, matching the estimations from observations.

Karlsson et al. (2015) suggested that jets, especially their fast *paramagnetic* plasmoids associated with an increase of magnetic field magnitude, are SLAMS that have travelled from the foreshock region to the magnetosheath through the rippled shock. This was the case in the simulation run by Palmroth et al. (2018), where a SLAMS-type structure crossing the shock was observed as a jet. The formation of this jet is shown in Figure 8. Here we can also see the corrugated structure of the quasi-parallel shock. However, as SLAMS are magnetic transients, jets formed via this mechanism would be expected to feature enhanced magnetic fields which is not the case for a large fraction of magnetosheath jets (Plaschke et al., 2013; Archer and Horbury, 2013).

Not every jet is observed downstream of the quasi-parallel shock. Even though according to Archer and Horbury (2013), jets are associated with steadier IMF than usual, a small fraction of jets can result from solar wind discontinuities: abrupt rotations in the IMF orientation turning the shock from quasi-perpendicular to

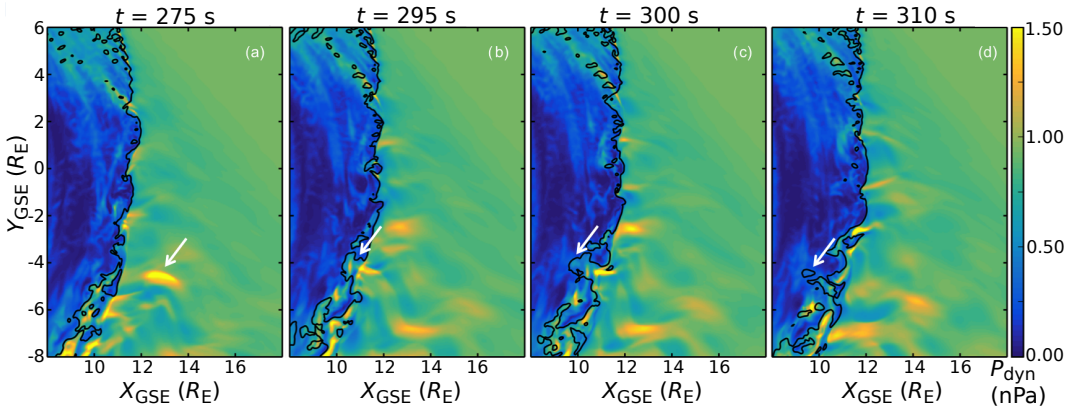

Figure 8. Snapshots showing the time evolution of a jet forming in the simulation run by Palmroth et al. (2018) from a SLAMS travelling through the shock (shown with the white arrows). The coloring represents the total dynamic pressure. The solar wind flows in the $-X$-direction and meets the bow shock at the boundary where the dynamic pressure decreases abruptly and the magnetosheath starts. The IMF cone angle is 30° and the foreshock region is at the bottom, where upstream dynamic pressure enhancements can be seen. The black contour corresponds to the Plaschke criterion of jet intervals: $P_{\mathrm{dyn,MSH},X} = \frac{1}{4} P_{\mathrm{dyn,\,SW}}$. The figure is adapted from Palmroth et al. (2018) and licensed under CC BY.

quasi-parallel or vice versa (Archer et al., 2012). Likewise, in the 2D simulations of Lin et al. (1996b) and Lin et al. (1996a), magnetosheath pressure pulses were formed when IMF rotational discontinuities interacted with the bow shock.

1.5.6 Observed effects

Magnetosheath jets interact with the surrounding plasma in the magnetosheath and can cause many types of effects when colliding into the magnetopause (Plaschke et al., 2018, and the references therein). These effects can be observed in the magnetosphere and sometimes even in the ionosphere. In Figure 9, the passage of jets from the bow shock to the magnetopause is illustrated along with some of the most prevalent jet-induced effects.

Plaschke and Hietala (2018) studied the flow patterns around jets using multi-spacecraft observations. They reported that jets accelerate the magnetosheath plasma in front of them and push the plasma to the side. In addition, ambient plasma behind the jet flows in to fill the wake left behind by the fast-moving jet.

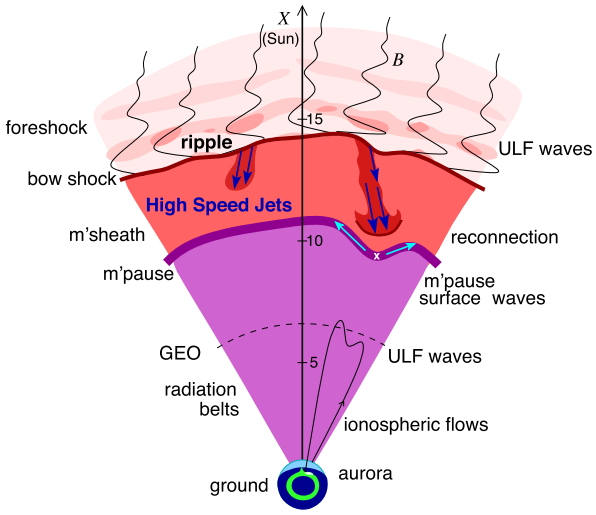

Figure 9. An illustration of jets originating from the rippled bow shock and possible effects in the magnetosphere and ionosphere following a jet hitting the magnetopause. The figure is from Plaschke et al. (2018) and licensed under CC BY.

Similarly, Plaschke et al. (2020) studied the effect of jets on the magnetosheath magnetic field. They found that jets alter the background magnetosheath magnetic field by dragging the field lines and aligning the field with their flow. However, they found the change in the median angle to be only 10°.

Due to the high dynamic pressure of jets, they have been observed to produce large indentations into the magnetopause when colliding into it (e.g, Amata et al., 2011; Archer et al., 2012; Hietala et al., 2009). Dmitriev and Suvorova (2012) showed that such indentations can also rebound in the opposite direction by reporting an event where the magnetopause expanded, compressed, and expanded again. In a recent study, Archer et al. (2019) observed a magnetosheath jet colliding into the magnetopause and exciting magnetopause standing surface waves, confirming the existence of magnetopause eigenmodes. Here, the jet set the dayside magnetic field lines into oscillating motion and the oscillations reflected from the ends of the field lines in the ionosphere.

As discussed before in Section 1.3, magnetic reconnection at the subsolar magnetopause is highly dependent on the orientation of the magnetic field on the side of the magnetosheath. Jets have been proposed to be able to locally affect mag-

netopause reconnection in multiple ways (Hietala et al., 2018): by impacting the magnetopause and making it thinner, by changing plasma beta (the ratio of plasma pressure and magnetic pressure) shear, or via altering the magnetic shear either by indenting the magnetopause or via the magnetic fields of jets themselves. Hietala et al. (2018) analyzed multi-spacecraft data and were able to provide observational evidence of an event where a jet triggered reconnection at the magnetopause. In this event the magnetic shear angle was already high but the magnetopause was unusually thick. The jet impact compressed the magnetopause until magnetic reconnection took place. Compression of the magnetopause increases the current density which is important for the diffusion of the magnetic field and for magnetic reconnection, as described in Section 1.3. Nykyri et al. (2019) recently studied an event where the IMF was northward but jets with southward $B_{Z,\mathrm{GSM}}$ were observed within the magnetosheath. They observed magnetic reconnection at the tail and suggested based on timing analysis that the jets may have triggered dayside magnetopause reconnection which ultimately led to the observed reconnection at the tail. Following these studies, we are interested in whether the magnetic field within jets statistically provides favorable conditions for affecting the occurrence of magnetic reconnection, either for enhancing or suppressing it.

Jets can also have effects inside the magnetosphere and on the ionosphere. Magnetopause surface waves drive magnetic field compressing ULF waves within the inner magnetosphere (Archer et al., 2013). The magnetopause indentations caused by jets compress the magnetosphere which may lead to acceleration of magnetospheric particles (Lee et al., 2016). Magnetospheric compressions could also lead to outer radiation belt electrons escaping into the magnetosheath (Plaschke et al., 2018). This has not yet been linked to jets but is typical during compression of the magnetopause. Jets have also been linked to transient density enhancements in the outer magnetosphere which could be associated with impulsive penetration of magnetosheath plasma into the magnetosphere (e.g. Gunell et al., 2012). Regarding ionospheric signatures, Hietala et al. (2012) reported enhanced flows in the

ionosphere that could be associated to increased particle precipitation into the ionosphere due to the magnetopause impacts of jets. Additionally, Wang et al. (2018) provided evidence for a direct link between jets and discrete and diffuse auroral brightenings.

The aforementioned phenomena are not exclusively consequences of magnetosheath jets but can also occur as consequences of solar wind discontinuities. Similarly, phenomena that have not yet been linked to jets but have been observed following solar wind discontinuities may be consequences of magnetosheath jets. It is clear that jets play a role in the transfer of solar wind energy and momentum into the magnetosphere. What is interesting about jets is that their occurrence and, therefore also the effects, are controlled by the orientation of the IMF. Here we will quantitatively study the IMF control of the spatial distribution of jets in more detail and estimate how often jets hit the subsolar magnetopause, as this is important for understanding the significance of their effects on the magnetosphere. We will specifically focus on the magnetic field within jets to understand how they might affect magnetic reconnection at the magnetopause.

2 Data and methods

In this chapter, we describe the data and the different models, coordinate systems, and statistical methods used in this thesis.

2.1 Observational data sets

We use the data set of Plaschke et al. (2013). Here, we concisely describe its characteristics. The measurements were made by the five THEMIS (Time History of Events and Macroscale Interactions during Substorms) spacecraft named A, B, C, D, and E during 2008–2011 (Angelopoulos, 2008). The THEMIS spacecraft orbit the Earth in highly elliptical orbits with different apogees. The data were gathered from the dayside subsolar magnetosheath within 7–18 R_{E} from the center of the Earth and within $\theta_{\mathrm{SZA}} < 30°$ (the angle between an Earth-centered position vector

and the Sun-Earth line). In this thesis, we use data from two instruments: the Fluxgate Magnetometer (FGM) (Auster et al., 2008) and the Electrostatic Analyzer (ESA) (McFadden et al., 2008). The measurements of different instruments were interpolated to a shared timeline with 1-second cadence.

The solar wind and interplanetary magnetic field data corresponding to the THEMIS observations were obtained from the high-resolution OMNI data set (King and Papitashvili, 2005). The OMNI data set is composed of multiple different spacecraft's measurements of the solar wind at different points and then extrapolated to the bow shock. To obtain representable values of the general solar wind and IMF conditions during the magnetosheath observations, the one-minute cadence OMNI data were averaged over the five minutes preceding the THEMIS measurements.

By requiring the density observed by THEMIS spacecraft to exceed twice the solar wind density, it was made sure that the spacecraft were not in the solar wind. Similarly, the energy flux of 10 keV ions was required to be smaller than that of 1 keV ions, to make sure the spacecraft were not in the magnetosphere where there are hot ion populations related to, e.g., magnetospheric currents. Taking all the magnetosheath data intervals longer than two minutes and with all the necessary quantities available, Plaschke et al. (2013) ended up with 2,736.9 hours of magnetosheath data. Finally, the jets were identified from the magnetosheath data with the criteria described in Section 1.5.2 and illustrated in Figure 5, yielding 2,859 jets and a total of 125,897 data points in these jet intervals.

2.2 GIPM coordinate system

As the orientation of the interplanetary magnetic field determines the locations of the quasi-parallel and quasi-perpendicular regions of the bow shock, it is helpful to move to a plane which contains the IMF vector and map the observations in this plane. This allows us to easily compare the locations of jet observations to the location of the quasi-parallel shock. For this purpose, we have chosen to use the Geocentric InterPlanetary Medium coordinate system (GIPM), first described by

Bieber and Stone (1979) and later used, e.g., by Verigin et al. (2006) and Dimmock and Nykyri (2013) in magnetosheath studies. In this Earth-centric frame, shown in Figure 10, the X_{GIPM}-axis is anti-parallel to the solar wind velocity vector, with orbital aberration taken into account, i.e., with the Earth's $\sim 30\,\mathrm{km/s}$ orbital motion removed. The Y_{GIPM}-axis is in the plane that contains the IMF and the X_{GIPM}-axis, that is, basically in the $\mathbf{B}_{\mathrm{IMF}}$–$\mathbf{V}_{\mathrm{SW}}$-plane. The GIPM unit vectors in GSE coordinates (described in Section 1.4) can be derived as functions of $\mathbf{V}_{\mathrm{SW}} = (V_X, V_Y, V_Z)$ and $\mathbf{B}_{\mathrm{IMF}} = \mathbf{B} = (B_X, B_Y, B_Z)$ (Verigin et al., 2006):

$$\hat{\mathbf{X}}_{\mathrm{GIPM}} = \frac{(-V_X, -V_Y - 30\ \mathrm{km/s}, -V_Z)}{\sqrt{V_X^2 + (V_Y + 30\ \mathrm{km/s})^2 + V_Z^2}} \tag{12}$$

$$\hat{\mathbf{Y}}_{\mathrm{GIPM}} = \begin{cases} \dfrac{(-\mathbf{B} + (\mathbf{B}\cdot\hat{\mathbf{X}}_{\mathrm{GIPM}})\hat{\mathbf{X}}_{\mathrm{GIPM}})}{|\mathbf{B} - (\mathbf{B}\cdot\hat{\mathbf{X}}_{\mathrm{GIPM}})\hat{\mathbf{X}}_{\mathrm{GIPM}}|}, & \text{if } \mathbf{B}\cdot\hat{\mathbf{X}}_{\mathrm{GIPM}} > 0 \\ \dfrac{(\mathbf{B} - (\mathbf{B}\cdot\hat{\mathbf{X}}_{\mathrm{GIPM}})\hat{\mathbf{X}}_{\mathrm{GIPM}})}{|\mathbf{B} - (\mathbf{B}\cdot\hat{\mathbf{X}}_{\mathrm{GIPM}})\hat{\mathbf{X}}_{\mathrm{GIPM}}|}, & \text{if } \mathbf{B}\cdot\hat{\mathbf{X}}_{\mathrm{GIPM}} < 0 \end{cases} \tag{13}$$

$$\hat{\mathbf{Z}}_{\mathrm{GIPM}} = \hat{\mathbf{X}}_{\mathrm{GIPM}} \times \hat{\mathbf{Y}}_{\mathrm{GIPM}}. \tag{14}$$

In the GIPM frame, the IMF cone angle between the X_{GIPM}-axis and the IMF is defined as

$$\alpha_{\mathrm{GIPM}} = \arccos\left(|\mathbf{B}\cdot\hat{\mathbf{X}}_{\mathrm{GIPM}}|/B\right) \in [0^\circ, 90^\circ]. \tag{15}$$

This angle always opens toward the quadrant where $X_{\mathrm{GIPM}} > 0$ and $Y_{\mathrm{GIPM}} < 0$, meaning that as the IMF cone angle grows, the quasi-parallel bow shock moves toward the negative part of the Y_{GIPM}-axis as can be seen in Figure 3. Therefore, by examining their Y_{GIPM}-coordinates, we can compare the occurrence of magnetosheath jets downstream of the quasi-parallel and quasi-perpendicular shock regions.

We separate the data into three subsets by the IMF cone angle: $\alpha_{\mathrm{GIPM}} \in [0^\circ, 30^\circ)$ representing quasi-radial IMF, $\alpha_{\mathrm{GIPM}} \in [30^\circ, 60^\circ)$ representing oblique IMF, and $\alpha_{\mathrm{GIPM}} \in [60^\circ, 90^\circ]$ representing high cone angle IMF. We chose these limits because the location of the quasi-parallel bow shock region varies considerably between these three cases, as can be seen in Figure 3. The subsolar magnetosheath can be considered to be downstream of the quasi-parallel shock during quasi-radial IMF and

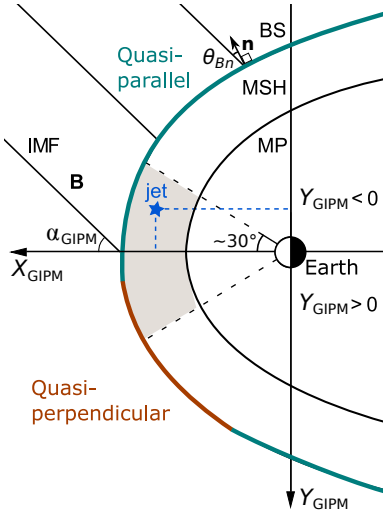

Figure 10. An illustration of the GIPM reference frame. The X_{GIPM}-axis is anti-parallel to the solar wind velocity and the Y_{GIPM}-axis is defined such that the X_{GIPM}–Y_{GIPM}-plane contains the IMF and the cone angle opens toward negative side of the Y_{GIPM}-axis. The observation area within the subsolar magnetosheath is sketched in grey. The figure is adapted from Vuorinen et al. (2019) and licensed under CC BY.

downstream of the quasi-perpendicular shock during high cone angle IMF. During oblique IMF, the subsolar magnetosheath is downstream of both, so that the quasi-parallel region is more on the negative side of Y_{GIPM}. These cone angle ranges also contain sufficient numbers of jet observations: 970, 1,403, and 486, respectively. The median values of the IMF cone angle within each range were 21.4°, 47.3°, and 75.2°.

2.3 Normalization methods

2.3.1 Normalization of spacecraft positions by the solar wind dynamic pressure

As explained in Section 1.2, the dynamic pressure of the solar wind affects the global size of the magnetosphere-bow shock system. We compare observations made during solar wind conditions that differ from one another, so we have to normalize the observed spacecraft positions. For this purpose, we apply the widely used relation (e.g., Spreiter et al., 1966; Formisano, 1979; Merka et al., 2005):

$$r_{\mathrm{norm}} = r_{\mathrm{obs}} \left(\frac{P_{\mathrm{dyn,SW,obs}}}{\overline{P}_{\mathrm{dyn,SW}}} \right)^{1/6} . \tag{16}$$

Here, the normalized distance r_{norm} from the Earth is obtained by scaling the measured distance r_{obs}, which was observed when the solar wind dynamic pressure was $P_{\mathrm{dyn,SW,obs}}$, by the data set average of the solar wind dynamic pressure: $\overline{P}_{\mathrm{dyn,SW}} = 1.76\,\mathrm{nPa}$ (assuming protons only).

2.3.2 Renormalization by all magnetosheath observations

Since the spacecraft have spent different amounts of time in different locations, in order to get the real observed occurrence rates of jets, we have to relate the number of observed jets to the total number of magnetosheath observations made in that particular region. Taking the durations of observation intervals into account, we can also obtain units of jets per unit time.

2.4 Bow shock and magnetopause models

We study the magnetic field within jets at different distances from the magnetopause. For that purpose, we use bow shock and magnetopause models to calculate the relative radial positions of the spacecraft between the magnetopause ($F = 0$) and the bow shock ($F = 1$):

$$F = (r - r_{\mathrm{MP}})/(r_{\mathrm{BS}} - r_{\mathrm{MP}}). \tag{17}$$

Here, r is the radial distance of the spacecraft measured from the center of the Earth, and r_{MP} and r_{BS} are the distances of the magnetopause and the bow shock, respectively, along that same line. The models contain some uncertainty and some magnetosheath observations do not fit between the expected bow shock and the magnetopause locations. Therefore, when we use the relative positions, we neglect observations that are not contained within the range $F \in [-0.1, 1.1]$. 3 % of jet interval observations and 5 % of non-jet magnetosheath observations are outside of these limits. We also use these models for visualization purposes when presenting two-dimensional distributions of jets in the X_{GIPM}–Y_{GIPM}-plane. Both of the following models are empirical models, i.e., they are based on observed bow shock or magnetopause crossings.

2.4.1 Merka et al. (2005) bow shock model

The bow shock models were published by Merka et al. (2005). When determining the distances of observations from the bow shock, we use the model made for the Geocentric Plasma Ecliptic coordinate frame (GPE) which is the GSE frame rotated in the XY-plane such that the solar wind flows anti-parallel to the X-axis (Merka and Szabo, 2004). The frame also corrects for the orbital motion of the Earth. The model bow shock is calculated for each measurement separately using the prevailing solar wind quantities at that time.

For visualization, we use the GIPM frame model and plot different curves for each cone angle range. The input parameters of the model are the solar wind dynamic pressure, for which we use the mean of the whole data set $\overline{P}_{\mathrm{dyn,SW}} = 1.76\,\mathrm{nPa}$, and the Alfvén Mach number M_{A} (using magnetic field magnitude $|B|$) for which we have calculated the means for each cone angle subset: 11.5, 9.92, and 9.74 (from the lowest to the highest cone angles).

2.4.2 Shue et al. (1998) magnetopause model

The model magnetopauses are based on the model presented by Shue et al. (1998). For the distance calculations, we use the original model that is rotationally symmetric around the X_{GSM}-axis corrected for orbital motion. Again, we calculate the model for each observation separately. When using the model for visualization, we plot the model around the X_{GIPM}-axis which is anti-parallel to the aberration-corrected solar wind velocity. This is justified since the solar wind velocity is almost radial and we only use the models for visualization. In this case, the input parameters for the models are the solar wind dynamic pressure, for which we use $\overline{P}_{\mathrm{dyn,SW}} = 1.76\,\mathrm{nPa}$, and the medians of IMF $B_{Z,\mathrm{GSM}}$ for each cone angle: $0.066\,\mathrm{nT}$, $-0.143\,\mathrm{nT}$, and $0.332\,\mathrm{nT}$.

2.5 Statistical methods

2.5.1 Confidence intervals

When studying the spatial distribution of jets and the magnetic field distributions of jets, we want to estimate the uncertainty of these results. We estimate the errors with 95 % significance level ($\lambda = 0.05$ error rate) binomial proportion confidence intervals using the Clopper-Pearson method (e.g., Brown et al., 2001), which is regarded as a conservative method. The lower and upper limits of the confidence interval $[p_{\text{lower}}, p_{\text{upper}}]$ are, respectively, the solutions of p corresponding to the following equations:

$$\Pr_p(X \geq x) = \lambda/2 \tag{18}$$

$$\Pr_p(X \leq x) = \lambda/2, \tag{19}$$

where $X \sim \text{Bin}(N, p)$, x is the number of successes, N is the number of trials, and p is the probability of success for each trial.

2.5.2 Estimating the magnetopause impact rates

We estimate how often jets hit the subsolar magnetopause during different IMF orientations using the model presented by Plaschke et al. (2016). Here, we will briefly describe the key points and ideas of the model. The model has been developed using multi-spacecraft jet observations within the Plaschke et al. (2013) data set, which is also used in this thesis. The model is based on the distribution of jet diameters $D_\perp$ in the direction perpendicular to their flow direction. This distribution can be estimated by looking at what nearby spacecraft observed in the plane perpendicular to the jet propagation direction. The data set includes 662 jet observations where there was a second spacecraft in this plane. A total of 655 of them were observed by THEMIS A, D, and E which orbit closer to the Earth and to the magnetopause than THEMIS B and C. Due to this, we only use data gathered by these spacecraft when estimating the magnetopause impact rates. As Plaschke et al. (2013) have

shown before, jets are more common close to the bow shock (Figure 6a). Thus, in order to get representable estimations of the impact rates, we need to use data from close to the magnetopause.

Plaschke et al. (2016) looked at the two-spacecraft observations as a function of the separation distance between the two spacecraft. They investigated how common it is that two spacecraft at given separations both see the same jet, as these probabilities allow us to deduce information about the sizes of the jets. Based on these fractions, they found that the observations could not be explained with a constant perpendicular jet diameter $D_\perp$, but found a good fit with an exponential probability distribution $P_\perp$ of $D_\perp$:

$$P_\perp = \exp\left(-D_\perp / D_{\perp 0}\right) / D_{\perp 0}, \tag{20}$$

with $D_{\perp 0} = 1.34\,R_\mathrm{E}$.

Multiplying the total number of observed jets per unit time (Q_obs) with the probability distribution $P_\perp$ and integrating over the perpendicular sizes $D_\perp$, they could calculate the observation rates of jets within a given size range defined by the integration limits. As these estimations were made based on observations close to the magnetopause, they assumed that these jets will also impact the magnetopause. When calculating the estimated number of jets impacting on the whole reference area A_ref of the subsolar magnetopause, they had to correct for the jets that were not observed by the spacecraft because, naturally, the spacecraft cannot observe all jets hitting this area as a spacecraft is measuring at a single point. They did the correction by calculating that the probability that a spacecraft sees the jet is the ratio of the jet area (projected onto the reference area) A_jet and the reference area A_ref. They used $A_\mathrm{ref} = 102\,R_\mathrm{E}^2$ which is a circular area perpendicular to the Sun-Earth line limited by $\theta_\mathrm{SZA} = 30°$ and the average radial distance $11.4\,R_\mathrm{E}$ of the observations. The final formula (see Plaschke et al. (2016) for a detailed derivation)

for the impact rate of jets larger than $D_{\perp\min}$ on the reference area $A_{\rm ref}$ is:

$$Q_{\rm imp} = \int_{D_{\perp\min}}^{\infty} \frac{A_{\rm ref}}{A_{\rm jet}} Q_{\rm obs} P_{\perp} \mathrm{d}D_{\perp} \tag{21}$$

$$= \frac{4A_{\rm ref}\cos\phi Q_{\rm obs}}{\pi D_{\perp 0}} \int_{D_{\perp\min}}^{\infty} e^{-D_{\perp}/D_{\perp 0}} \frac{\mathrm{d}D_{\perp}}{D_{\perp}^2}. \tag{22}$$

Here ϕ is the mean angle between the jet propagation direction and the $-\hat{\mathbf{X}}_{\rm GSE}$ unit vector. In this thesis, the input values for $Q_{\rm obs}$ and ϕ during different IMF orientations are from lowest to highest cone angle range: $2.93\,\mathrm{h}^{-1}$ & 25.7°, $1.26\,\mathrm{h}^{-1}$ & 24.7°, and $0.261\,\mathrm{h}^{-1}$ & 23.8°.

2.5.3 Kolmogorov-Smirnov test

We compare the magnetic field within jets to the magnetic field within the non-jet magnetosheath in Section 3.2. For this purpose, we use a non-parametric test to validate our results. We use the two-sample Kolmogorov-Smirnov test (KS2-test) to test whether two samples are from the same continuous distribution (e.g., Press et al., 2007). This test can be applied without knowing the underlying distribution, as it compares the empirical cumulative distribution functions (CDFs) of the two samples. The test statistic is the maximum absolute difference between the two CDFs $S_{N_1}(x)$ and $S_{N_2}(x)$ of the independent variable x:

$$D = \max_{x} \left| S_{N_1}(x) - S_{N_2}(x) \right|. \tag{23}$$

The null (alternative) hypothesis of the test is that the two samples are from the same (different) continuous distributions.

2.5.4 Spearman rank-order correlation coefficient

We also calculate the correlation between the IMF and the magnetic field in the magnetosheath and within jet intervals using the Spearman rank-order coefficient. This correlation coefficient r_s measures the ordinal correlation between two variables x and y (Press et al., 2007). The data of each variable are ranked from the lowest value (rank 1) to the highest value (rank W = number of data points) so that each

pair (x_i, y_i) corresponds to a rank-pair (R_i, S_i). The correlation coefficient is then calculated as the Pearson correlation coefficient that measures linear correlation between the ranks R and S. The formula for Spearman rank-order correlation coefficient becomes (Press et al., 2007):

$$r_s = \frac{\sum_i (R_i - \overline{R})(S_i - \overline{S})}{\sqrt{\sum_i (R_i - \overline{R})^2}\sqrt{\sum_i (S_i - \overline{S})^2}}. \tag{24}$$

$r_s = 0$ indicates no linear rank correlation and values 1 and -1 indicate complete positive and negative linear rank correlation, respectively (Press et al., 2007).

2.5.5 Generating magnetosheath samples following similar solar wind distributions as the jets

After classifying the jets based on their relative position between the magnetopause and the bow shock (as described in Section 2.4), we compare the magnetic field within jets to the corresponding non-jet magnetosheath magnetic field observations. As already reported by, e.g., Plaschke et al. (2013) and Archer and Horbury (2013), jet occurrence is strongly controlled by one parameter: the IMF cone angle, as jets occur preferentially during low cone angle IMF. Therefore, it can be assumed that the magnetic field within jets is probably different than the average magnetosheath magnetic field simply due to the fact that the IMF conditions were different, on average. Furthermore, in our data set, jets closer to the magnetopause tend to be observed during lower cone angle conditions than those observed closer to the bow shock (A. LaMoury, private communication). To take this into account, we generate samples of non-jet magnetosheath observations that follow the same IMF cone angle distribution as the jets observed at the same relative position range between the bow shock and the magnetopause.

We apply the widely-used method of *inverse transform sampling* (e.g., Ross, 2013). The samples are obtained as follows. We start by computing the CDFs of the relative radial positions (Figure 6a) and the IMF GSE cone angles (Eq. (15), but using GSE vectors; Figure 6b) for the jet interval observations. For the relative

positions we take the CDF over $F \in [-0.1, 1.1]$ with a bin width of 0.2, and for the cone angles $[0°, 90°]$ we used a bin width of 5°. Our results were not very sensitive to these selections. As a CDF gets values from $[0, 1]$, we can generate random samples from the distribution by generating uniformly distributed pseudorandom numbers $(0, 1)$ with a Mersenne Twister generator (MathWorks^{TM}, 2018). Each random number corresponds to a bin in the discrete CDF. First, we draw a relative position bin and sample the cone angle bin from the cone angle distribution of that bin. Then we look for all non-jet magnetosheath observations belonging to both of these bins and randomly select one of these observations. This process is repeated until we have the sample size that we want.

We also compare the minima and maxima of the jet intervals to those of similar non-jet magnetosheath intervals. The non-jet intervals are obtained by first sampling one observation for that interval, following the relative position and IMF cone angle distributions of jet t_0 (moment of the highest dynamic pressure) measurements. Then subsequent (or preceding) magnetosheath observations are added to the interval until we have the desired interval length. The distribution of jet interval lengths does not vary very much for different relative positions in the magnetosheath so we always sample the interval length from the distribution of all jet interval lengths.

3 Results

In this chapter, we present the results of our study in two parts. First, in Section 3.1, we look at how the IMF orientation controls where magnetosheath jets occur and how often these jets impact the subsolar magnetopause. These results have been previously published in Vuorinen et al. (2019). Secondly, in Section 3.2, we present the results on the magnetic field within the jet intervals and evaluate whether jets could enhance or suppress magnetic reconnection at the subsolar magnetopause.

3.1 IMF control of jet occurrence and magnetopause impact rates

In Figure 11, we present the spatial occurrence rates of jets for the three different IMF orientations, from quasi-radial to high cone angle IMF, as functions of Y_{GIPM} and Z_{GIPM}. The observations have been normalized to $\overline{P}_{\mathrm{dyn,SW}} = 1.76\,\mathrm{nPa}$ and renormalized by the distribution of all magnetosheath observations, as described in Section 2.3. The jet observations are the data points corresponding to the time t_0 within the jet interval, that is, the moment of the highest dynamic pressure. Due to their large uncertainties, we have left out the outermost bins for Y_{GIPM} containing two (0.07 %) jets and 3,984 (0.04 %) magnetosheath observations in total, and for Z_{GIPM} 1,465 (0.01 %) magnetosheath observations. We can see clear differences in the three histograms for both coordinates, as expected based on previous studies (Archer and Horbury, 2013; Plaschke et al., 2013, Figure 6b). The jet occurrence is the highest for quasi-radial IMF ($\alpha_{\mathrm{GIPM}} \in [0°, 30°)$; in blue) and lowest for high cone angle IMF ($\alpha_{\mathrm{GIPM}} \in [60°, 90°]$; in orange). The quasi-radial IMF corresponds to the subsolar magnetosheath being mostly downstream of the quasi-parallel shock and the high cone angle IMF downstream of the quasi-perpendicular shock.

In the case of Y_{GIPM} positions in Figure 11a, the distributions vary in shape. The distribution for quasi-radial IMF is quite flat with a little bit higher occurrence rates on the negative side of the Y_{GIPM}-axis, although this is within the error bars. Overall, during quasi-radial IMF the number of observed jets is around 1–2 per hour per R_{E}. For the case of high cone angle IMF, the distribution is flat with an approximate occurrence rate of a jet observed once in five hours per R_{E}. Taking the average of the six bins in the middle with moderate error bars for these two cone angle ranges, we calculate that jets occur 9 times more often during quasi-radial IMF than during high cone angle IMF. The error bars give this factor limits of 6–14. The case in between, corresponding to oblique IMF (in purple) with intermediate cone angles $\alpha_{\mathrm{GIPM}} \in [30°, 60°)$, looks very different. The occurrence rates clearly

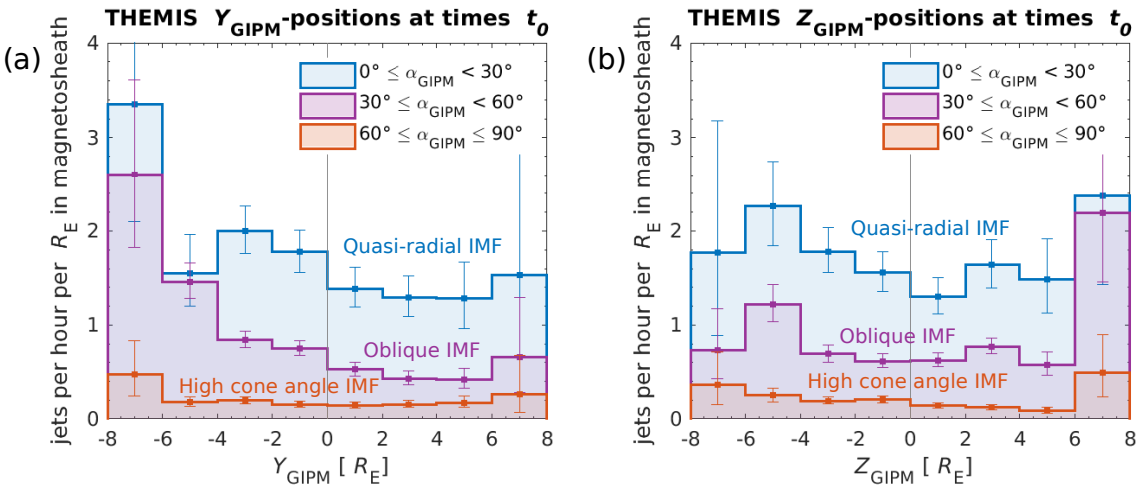

Figure 11. Histograms presenting the numbers of observed jets per hour per R_E in the subsolar magnetosheath as functions of (a) Y_{GIPM} and (b) Z_{GIPM} (normalized to $\overline{P}_{dyn,SW} = 1.76\,nPa$) during the three different IMF orientations. The error bars represent 95 % binomial proportion confidence intervals obtained by the Clopper-Pearson method. Figure (a) is adapted from Vuorinen et al. (2019) and licensed under CC BY.

increase when Y_{GIPM} decreases, and this increase seems to be monotonous. The distribution meets that of quasi-radial IMF in the negative end of the Y_{GIPM}-axis and likewise that of high cone angle IMF in the positive end of the Y_{GIPM}-axis.

Looking at the Figure 11b, the distributions of Z_{GIPM} positions have a more or less flat shape for all three IMF orientations, within the error bars. As an exception, the rightmost bin $[6\,R_E, 8\,R_E]$ for the oblique IMF is interestingly high, with the occurrence rate almost matching that of the quasi-radial IMF. However, the uncertainties in these bins are high, and statistically more reliable results for these regions can be obtained when more data is available. All in all, there does not seem to be a clear dependence on Z_{GIPM} for jet occurrence.

In Figure 12, we present 2D maps of the more interesting case, the X_{GIPM}–Y_{GIPM}-plane. The jet observations have again been normalized by the mean solar wind pressure 1.76 nPa and renormalized by the distribution of all magnetosheath observations. The maps consist of $2\,R_E \times 2\,R_E$ squares but we neglect cells with fewer than 1,000 magnetosheath observations. Furthermore, cells with $\geq$ 1,000 magnetosheath observations but with no jets are notated with white cells with dashed outlines. We

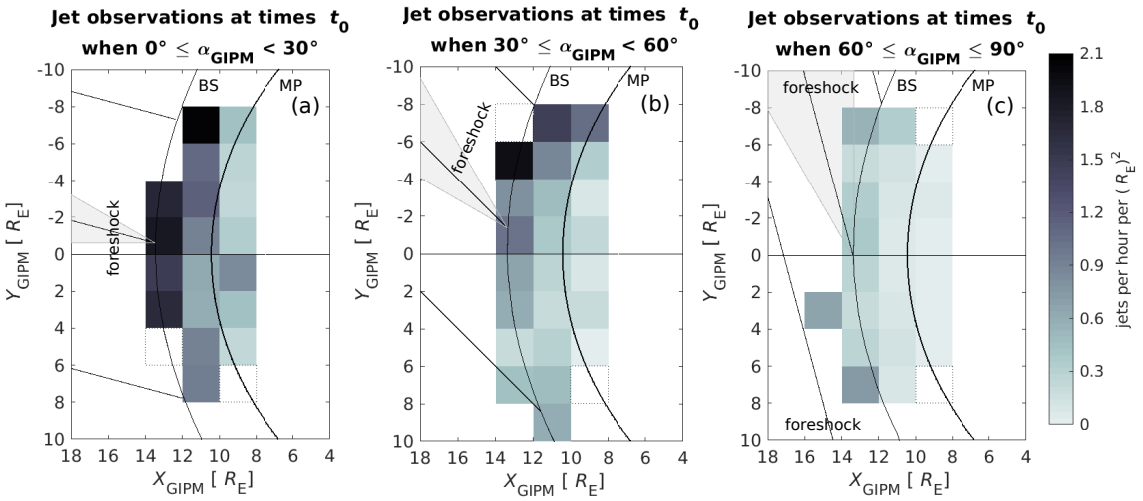

Figure 12. 2D maps presenting the numbers of observed jets per R_{E}^2 as functions of X_{GIPM} and Y_{GIPM} (normalized to $\overline{P}_{\mathrm{dyn,SW}} = 1.76\,\mathrm{nPa}$) during the three different IMF orientations: (a) quasi-radial, (b) oblique, and (c) high cone angle IMF. The squares with fewer than 1,000 magnetosheath observations are shown in white and the squares with more than that but zero jets are dashed. Magnetic field lines are plotted in the solar wind on the left and they represent the middle cone angle of each range. The grey cones represent the whole cone angle range. Model magnetopauses and bow shocks have been plotted as described in Section 2.4. The figure is adapted from Vuorinen et al. (2019) and licensed under CC BY.

immediately see that jets are most frequently observed close to the bow shock as reported before by Plaschke et al. (2013) and seen in Figure 6a. The same trends are visible as in Figure 11: jets are observed on the whole width of the Y_{GIPM}-axis during quasi-radial IMF, during oblique IMF jets mainly occur on the negative side of the axis and the number of jets all around the subsolar magnetosheath drops for high cone angle IMF. For the last case, the jet occurrence is higher on the edges of the Y_{GIPM}-axis as could be expected assuming that these areas are downstream of the edge of the quasi-parallel shock. However, as seen in Figure 11, the error bars are large in these regions. Similarly, the darker spot at $X_{\mathrm{GIPM}} = [14\,R_{\mathrm{E}}, 16\,R_{\mathrm{E}})$ and $Y_{\mathrm{GIPM}} = [2\,R_{\mathrm{E}}, 4\,R_{\mathrm{E}})$ only contains one jet leading to high uncertainty.

Next, we present the estimations of the magnetopause impact rates of three different sized (0.5–1.0 R_{E}, 1.0–2.0 R_{E}, and $> 2.0\,R_{\mathrm{E}}$) jets in Figure 13. As described in Section 2.5.2, these are sizes of jets perpendicular to their propagation

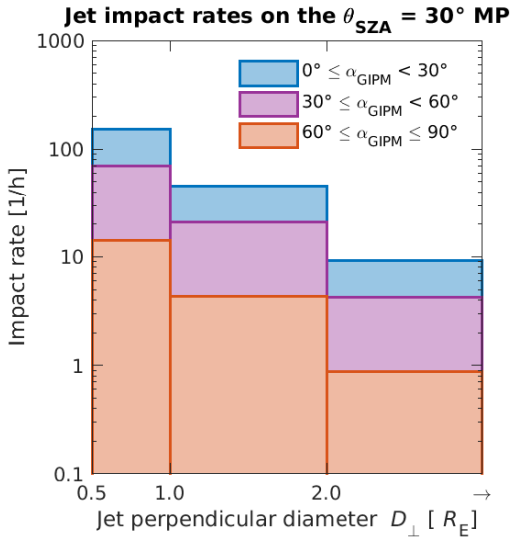

Figure 13. Estimations of the numbers of jets impacting the 30° solar zenith angle (SZA) subsolar magnetopause per hour for three size scales perpendicular to the jet propagation direction: 0.5–1.0 R_E, 1.0–2.0 R_E, and geoeffective jets > 2.0 R_E. These are presented separately for the three IMF cone angles. The figure is from Vuorinen et al. (2019) and licensed under CC BY.

direction. Plaschke et al. (2016) considered jets with perpendicular diameters larger than 2.0 R_E to be geoeffective, meaning that signatures of such jets colliding into the magnetopause can be observed at Earth. We find, similarly to Plaschke et al. (2016), that this type of geoeffective jets impact the magnetopause approximately 9.4 times per hour during quasi-radial IMF, 4.1 times per hour during oblique IMF and 0.85 times per hour during high cone angle IMF. Here, on top of those largest jets, we looked at smaller scale sizes as well. We find that jets larger than 1.0 R_E impact the magnetopause 5–56 times per hour depending on the IMF orientation. Jets smaller than that collide into the subsolar magnetopause much more frequently bringing the total impact rates of all sized jets up: 3.5 jets per minute during quasi-radial IMF and 0.31 jets per minute during high cone angle IMF.

3.2 Magnetic field within jets

In Figure 14, we present histograms of the magnetic field GSM components and magnitude within jet intervals (in blue) and non-jet magnetosheath observations (in red): these are visibly different. The KS2-test rejects the null hypotheses with

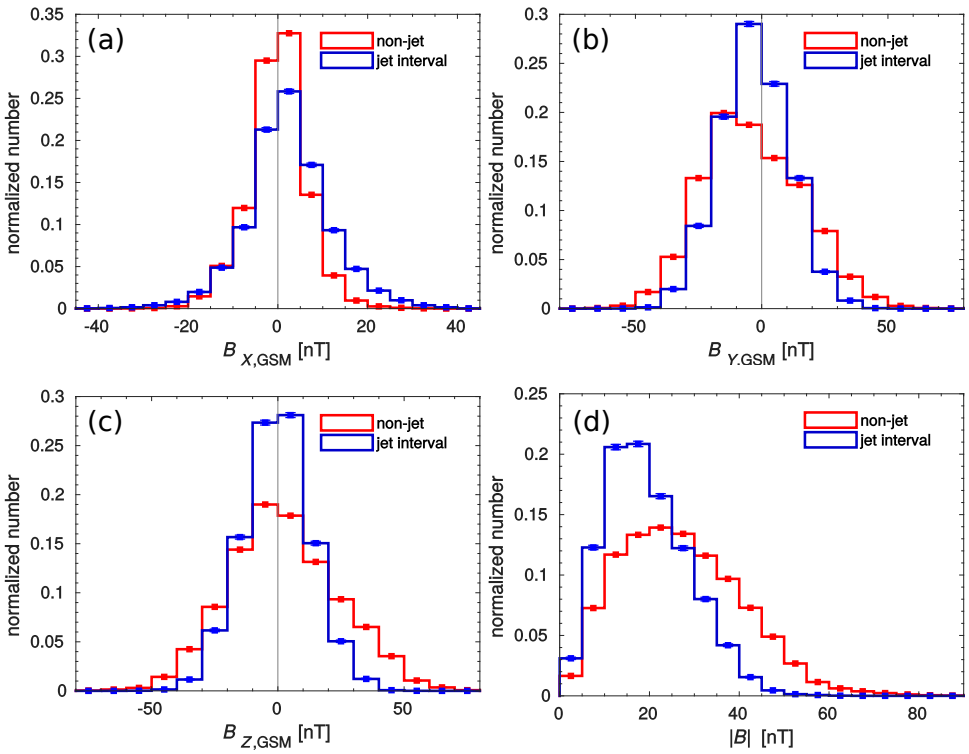

Figure 14. The distribution of jet interval and non-jet magnetosheath observations as a function of (a) $B_{X,\mathrm{GSM}}$, (b) $B_{Y,\mathrm{GSM}}$, (c) $B_{Z,\mathrm{GSM}}$, and (d) $|B|$. The error bars were calculated as 95 % binomial proportion confidence intervals with the Clopper-Pearson method.

		B_X	B_Y	B_Z	$\lvert B\rvert$
jet interval	mean	2.27 nT	−2.86 nT	−0.333 nT	19.5 nT
	median	1.93 nT	−3.05 nT	−0.161 nT	18.2 nT
	std	9.45 nT	13.6 nT	13.3 nT	9.30 nT
	skewness	0.037	0.048	−0.022	0.558
non-jet	mean	−0.022 nT	−3.54 nT	2.27 nT	27.1 nT
	median	0.199 nT	−5.30 nT	0.967 nT	25.8 nT
	std	6.54 nT	19.7 nT	21.7 nT	13.7 nT
	skewness	−0.120	2.34	0.198	6.93

Table 1. The means, medians, standard deviations, and skewnesses of B_X, B_Y, B_Z, and $|B|$ distributions of jet interval and non-jet observations in the GSM frame.

$p < 0.001$, indicating high significance, for all these quantities. This suggests that the underlying distributions of each of the quantities are not identical between the jet interval and the non-jet observations. The means, medians, standard deviations, and skewnesses of these data sets are presented in Table 1. As can also be seen in Figure 14a, the jet intervals have a larger variance in B_X than the non-jet magnetosheath. Conversely, we can also see in Figure 14b for B_Y and in Figure 14c for B_Z, that the

variances are larger within the non-jet magnetosheath. $|B|$ and its variance within our jet intervals tend to be smaller than within the non-jet magnetosheath. The results suggest that the magnetic field is statistically different within jet intervals compared to normal magnetosheath plasma. However, it should be noted that in order to make further conclusions from these comparisons, the distributions should be classified by relative position between the magnetopause and the bow shock and also by the upstream IMF conditions. All in all, these results give us confidence to study the fields further and, thus, we will look at the B_Z in more detail.

As discussed before, the B_Z component is important for magnetopause reconnection because it dominates the magnetic shear angle at the subsolar magnetopause between the magnetosheath magnetic field on one side and the northward ($B_Z > 0$) Earth's magnetic field on the other side. We also know that the IMF orientation influences the magnetosheath magnetic field, so we divide the data into two categories: northward IMF with $B^{\mathrm{IMF}}_{Z,\mathrm{GSM}} > 0$ and southward IMF with $B^{\mathrm{IMF}}_{Z,\mathrm{GSM}} < 0$. Note that the terms *southward* and *northward* are not strict here because we do not consider the other magnetic field components. In Figure 15, we present the B_Z distributions of jet interval and non-jet observations separately for these two categories. The means, medians, standard deviations, and skewnesses of both of these categories are presented in Table 2. We can see that the orientation of the IMF clearly affects the B_Z within the magnetosheath. During northward IMF, the jets and the non-jet magnetosheath tend to have more northward (positive) values of B_Z and vice versa. In fact, the Spearman rank-order correlation coefficient between B_Z in the non-jet magnetosheath and corresponding $B^{\mathrm{IMF}}_{Z,\mathrm{GSM}}$ in the solar wind is 0.7784 ($p < 0.001$) which indicates high positive rank correlation. For jet intervals, the corresponding value was 0.5257 ($p < 0.001$), indicating that the correlation between the IMF and the magnetic field B_Z in jets is not as strong as for the non-jet magnetosheath. The distributions during northward and southward IMF do not seem to be symmetric. We test this by using the KS2-test. The non-jet MSH distributions are not symmetrical according to the KS2-test that rejects the null hypothesis ($p < 0.001$). We

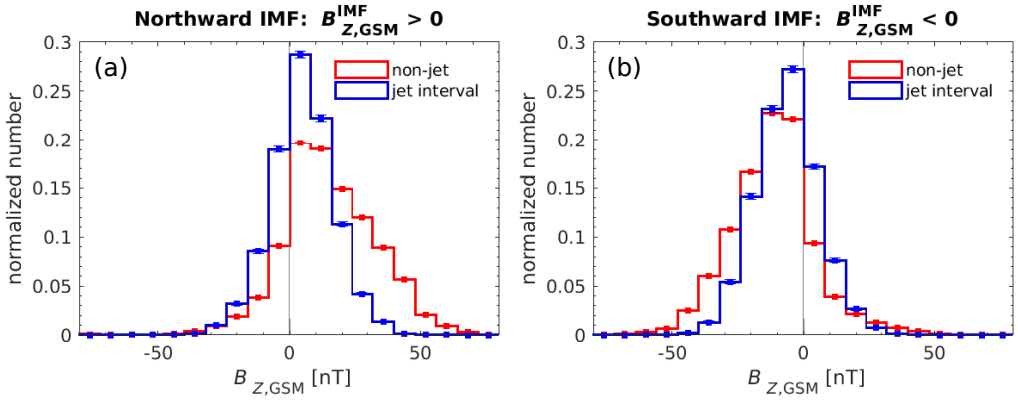

Figure 15. The magnetic field component $B_{Z,\mathrm{GSM}}$ for jet interval (blue) and non-jet (red) observations for (a) northward IMF ($B^{\mathrm{IMF}}_{Z,\mathrm{GSM}} > 0$) and (b) southward IMF ($B^{\mathrm{IMF}}_{Z,\mathrm{GSM}} < 0$). The confidence limits were calculated as 95 % binomial proportion confidence intervals with the Clopper-Pearson method.

can see that the non-jet distribution has higher absolute values during northward IMF than during southward IMF. The corresponding $B^{\mathrm{IMF}}_{Z,\mathrm{GSM}}$ distribution does not exhibit similar behaviour (medians: southward IMF -1.81 nT and northward IMF 1.83 nT), which indicates that the magnetosheath is most likely affected by the magnetic pile up layer that forms in front of the magnetopause during northward IMF. The jet interval distributions are not symmetric either (null hypothesis rejected with $p < 0.001$).

		B_Z	
		$B^{\mathrm{IMF}}_{Z,\mathrm{GSM}} > 0$	$B^{\mathrm{IMF}}_{Z,\mathrm{GSM}} < 0$
jet interval	mean	5.00 nT	-6.41 nT
	median	4.95 nT	-6.25 nT
	std	12.0 nT	12.1 nT
	skewness	-0.101	0.101
non-jet	mean	15.4 nT	-11.7 nT
	median	13.7 nT	-11.3 nT
	std	17.7 nT	16.2 nT
	skewness	0.099	0.427

Table 2. The means, medians, standard deviations, and skewnesses of $B_{Z,\mathrm{GSM}}$ distributions of jet interval and non-jet observations during northward and southward IMF.

With the aim to study whether jets could affect magnetic reconnection at the magnetopause, next we will consider how the B_Z distribution changes as we move from the bow shock toward the magnetopause. Before that, however, it is important

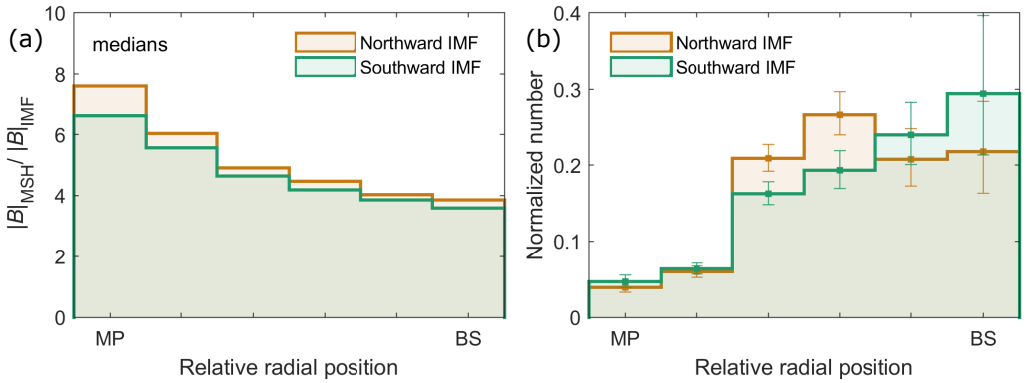

Figure 16. (a) The medians of non-jet magnetosheath field magnitude normalized by the IMF magnitude as functions of the relative radial position between the MP and BS during northward and southward IMF. (b) The relative radial positions of jet t_0 observations from the Earth during southward and northward IMF normalized by the distribution of all MSH observations. The error bars were calculated as 95 % binomial proportion confidence intervals with the Clopper-Pearson method.

to investigate whether jets can make it to the magnetopause across the magnetic pile-up layer. In Figure 16a, we have plotted the medians of non-jet magnetosheath magnetic field magnitude normalized by the upstream field magnitude during northward and southward IMF as functions of relative position between the magnetopause and the bow shock. It can be seen that the magnetic flux does pile up in front of the magnetopause more strongly during northward IMF. To test whether this affects the occurrence of jets, in Figure 16 we present the relative positions of the spacecraft between the magnetopause and the bow shock at times t_0, normalized by all MSH observations, separately for northward and southward IMF. It seems that jets are observed just as frequently close to the magnetopause during these two IMF conditions, suggesting that jets can penetrate through the magnetic pile-up layer.

In Figure 17, we present the distributions of B_Z within jet intervals and non-jet magnetosheath samples as functions of relative position, again separately for northward and southward IMF. The non-jet magnetosheath samples have been generated by creating samples of the same size as the jet samples and following jets' distributions of relative positions and IMF cone angles, as explained in Section 2.5.5. The distributions are displayed using their 10^{th}, 50^{th} (medians), and 90^{th} percentiles. To

evaluate the effect of finite sample size, we created several non-jet samples, averaged their percentiles, and calculated their standard deviations (σ). We investigate the distributions of all jet interval data points in Figures 17a & 17b compared to the average percentiles of three same sized non-jet magnetosheath samples (individually sampled observations, not intervals). Jet interval minima in Figures 17c & 17d and jet interval maxima in Figures 17e & 17f are compared to minima and maxima, respectively, averaged from 100 samples consisting of non-jet magnetosheath intervals similar to the jet intervals. We do this to get a good picture of the variations of B_Z within the jet intervals and how these variations compare to the inherent background variations.

The effect of field lines becoming tangential to the magnetopause is visible in Figures 17a & 17b, as the B_Z distribution of non-jet observations broadens toward to the magnetopause. The direction of this broadening follows the direction of the IMF, so that during northward IMF (Figure 17a) the tangential field lines tend to point northward and vice versa (Figure 17b). We can see that in the leftmost bin ($F \in [-0.1, 0.1)$) next to the magnetopause, during northward IMF the B_Z distribution exhibits larger absolute values (median: 17 nT, $\sigma = 0.084$ nT) than during southward IMF (median: -12 nT, $\sigma = 0.20$ nT) due to the formation of the magnetic pile-up layer caused by the lack of reconnection. The jet interval distributions also broaden but not as much suggesting that jets seem to be able to maintain their magnetic properties better than the background while propagating in the magnetosheath. The medians of jet interval observations next to the magnetopause are also different in magnitude: 6 nT for northward and -11 nT for southward IMF.

Let us look at the leftmost bin in more detail because the magnetic field right next to the magnetopause is important from the perspective of reconnection. In Figure 17a, we can see that during northward IMF, jets exhibit lower values of B_Z (median: 6 nT) than the non-jet magnetosheath (median: 17 nT, $\sigma = 0.084$ nT). Jet intervals also have negative, or southward, values of B_Z more often: 36 % and 21 % ($\sigma = 0.021$ %) of the time, respectively. Thus, southward fields are relatively

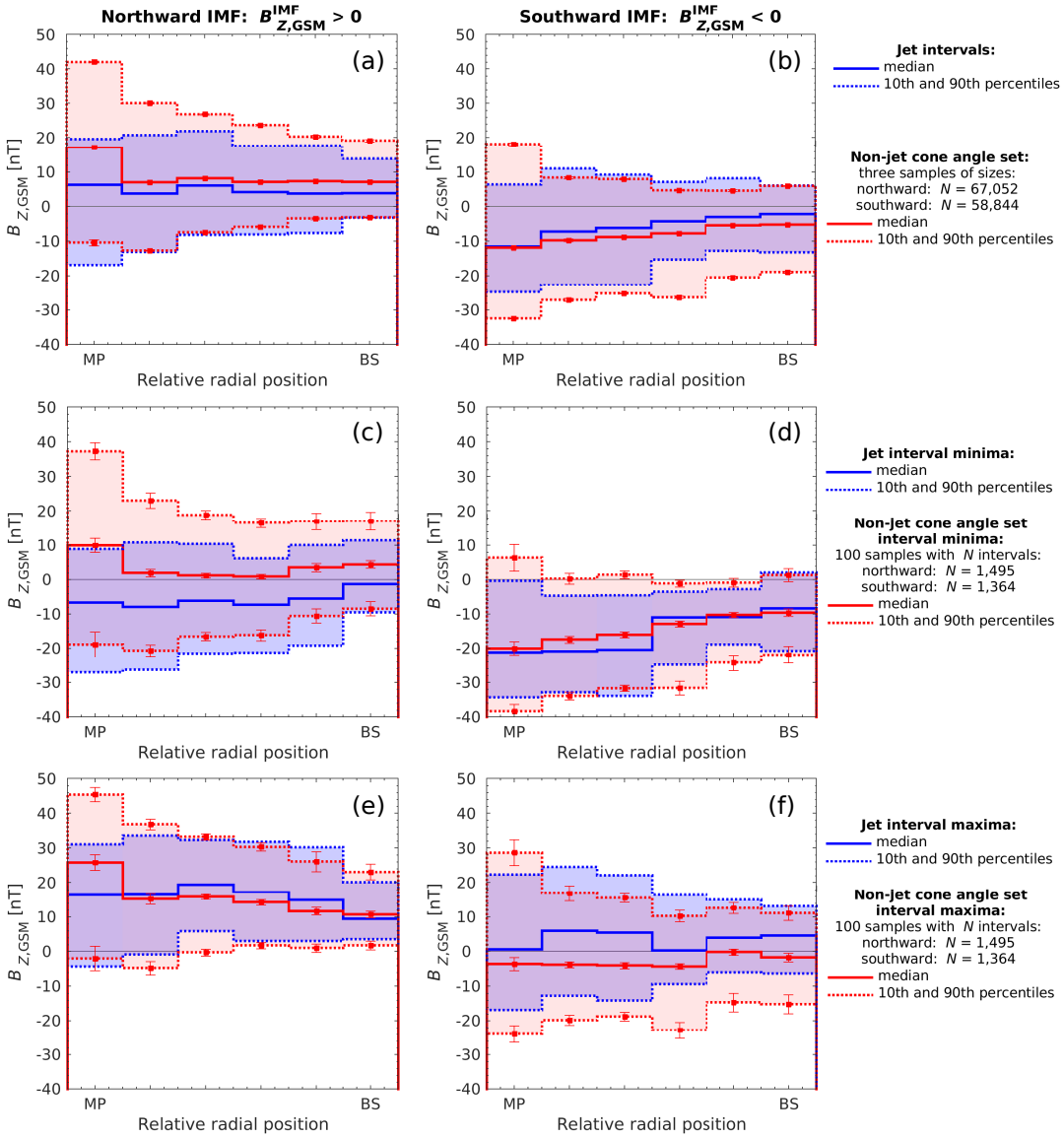

Figure 17. The 10^{th}, 50^{th} (medians), and 90^{th} percentiles of the magnetic field component $B_{Z,\text{GSM}}$ as a function of relative radial position between the magnetopause and the bow shock. All jet interval observations compared to averages of three non-jet cone angle samples during (a) northward and (b) southward IMF. Minima ((c) northward and (d) southward IMF) and maxima ((e) northward and (f) southward IMF) of the jet intervals and averages of 100 non-jet cone angle samples of similar intervals. The error bars represent the standard deviations (σ) of the averaged percentiles.

more common within jets and jets tend to have larger absolute values of negative B_Z. During southward IMF (Figure 17b), the jet interval and the sampled non-jet magnetosheath distributions have practically equal medians but the non-jet magnetosheath has a larger spread in both the positive and the negative ends of the

distribution, meaning that large absolute values of positive and negative B_Z are more common than within jets. 27 % ($\sigma = 0.15$ %) of non-jet observations and 18 % of jet interval observations had $B_Z > 0$. Therefore, southward B_Z is more common within jets than within the non-jet magnetosheath also during southward IMF, but the latter tends to exhibit stronger northward and southward fields.

In the distributions of the minima during northward IMF in Figure 17c, we have a much larger fraction of jet intervals exhibiting southward fields than similar magnetosheath intervals: 73 % and 30 % ($\sigma = 4.3$ %) of the intervals had southward magnetic field values within them, respectively. The medians of the interval minima were -7 nT for jets and 10 nT ($\sigma = 2.1$ nT) for non-jet intervals. During southward IMF (Figure 17d), the non-jet interval minima have a median of -21 nT ($\sigma = 1.7$ nT), almost equal to the median of jet interval minima. The variations at the tails of the distributions are very similar considering the error bars. The distributions of interval maxima during northward IMF (Figure 17e) show us that jets tend to have smaller values of maximum B_Z than the non-jet intervals, with medians 16 nT and 26 nT ($\sigma = 4.3$ nT), respectively. During southward IMF (Figure 17f), the distributions of jet and non-jet intervals maxima have medians 1 nT and -4 nT ($\sigma = 1.6$ nT), respectively. The medians and the variations at the tails are of a similar size when taking the error bars into account.

Overall, close to the magnetopause during northward IMF, southward fields are more common within jet intervals than in the non-jet magnetosheath. Furthermore, throughout the magnetosheath, it is significantly more likely for a jet to exhibit southward B_Z compared to similar non-jet intervals. This means that the changes introduced by jets are not simply comparable to the background variations but there is a systematic effect that is most pronounced next to the magnetopause. However, during southward IMF, the medians of the jet and non-jet distributions are very similar but non-jet magnetosheath has larger variations, indicating that the inherent variations of the magnetosheath are larger than the effects of jets.

4 Discussion

This chapter presents the caveats of the study and discussion on the results. We give our interpretations of the results and relate them to previous studies.

4.1 Caveats

The solar wind and IMF data used in this study are obtained from the OMNI data, which has been compiled of measurements made by multiple different satellites at L1 and time-shifted to the front of the Earth's bow shock (King and Papitashvili, 2005). The estimated time-shift contains some uncertainty, and the solar wind and IMF conditions can vary between the different spacecraft which may cause local bias. Furthermore, the solar wind structures may evolve while propagating toward the Earth. However, since OMNI data is gathered from multiple spacecraft and we have averaged the conditions over five preceding minutes, we can trust the data to give us a good picture of the general solar wind conditions.

The caveat of the GIPM frame is that when the IMF line is close to being parallel with the X_{GIPM}-axis, i.e., during very low cone angle IMF, the direction of $\hat{\mathbf{Y}}_{\mathrm{GIPM}}$ is not well-defined. Within our low cone angle range $\alpha_{\mathrm{GIPM}} \in [0°, 30°)$, only 20 % of jets occurred when $\alpha_{\mathrm{GIPM}} < 15°$. Therefore, we do not expect this to be a significant caveat. One must also note that the shock has curvature in the Z_{GIPM}-direction as well. This means that the local shock normals are not exactly in the X_{GIPM}–Y_{GIPM}-plane and θ_{Bn} is not determined by Y_{GIPM} only. However, this curvature is small in the subsolar region which we study, and therefore, this additional angular component to θ_{Bn} is small. Furthermore, Figure 11b suggests that there is no strong dependence on Z_{GIPM} confirming that this component is not important.

Regarding the jet impact rate estimations, the model created by Plaschke et al. (2016) makes an assumption that the distribution of jet perpendicular diameters is the same during all IMF orientations, which does not have to be true. As most of the jets used to derive the distribution were observed during IMF cone angles

20°–50°, the distribution is likely biased toward the size of such jets.

When looking at the distributions of magnetic field components and the field magnitude, we used all jet interval data points. This skews the distribution so that short-duration jets are under-represented. However, we see this as the best way to make comparisons between the magnetic field within jets and non-jet magnetosheath observations as no particular point within the jet should be special and the magnetic field within the jets is very variable. How the magnetic field changes within a jet interval has to be studied in the future.

The relative positions between the magnetopause and the bow shock determined from the models of Shue et al. (1998) and Merka et al. (2005), respectively, contain uncertainty. As noted earlier, 3 % of jets and 5 % of all magnetosheath observations did not fit the range we studied. Nevertheless, the B_Z distribution of the non-jet magnetosheath as a function of relative position between the magnetopause and the bow shock exhibits the expected signatures: draping and the magnetic pile-up layer. This gives us good confidence on the models.

Even though the $B_{Z,\mathrm{GSM}}$ within the magnetosheath is a good proxy for the magnetic shear angle at the magnetopause, the actual angle is also dependent on the X_{GSM} and Y_{GSM} components of the magnetic field. As reviewed by Cassak and Fuselier (2016), many studies have investigated whether magnetic reconnection requires strictly anti-parallel fields or whether so-called component reconnection exists, where only a component of the field reconnects. Observations at the dayside magnetopause have revealed that both component and anti-parallel reconnection do occur. However, most observations have been very close to anti-parallel, within the limits of measurement accuracy. According to a popular maximum shear model (Trattner et al., 2007), reconnection happens at the point where the magnetic shear is maximized. Moreover, magnetic reconnection is a very complex process and, although the magnetic shear angle is a very important parameter, it is not the only parameter affecting the process. Others include plasma beta shear between the two regions and the current sheet thickness, which we have not considered here.

4.2 Occurrence and magnetopause impacts of jets

Similarly to the results of Plaschke et al. (2013) and Archer and Horbury (2013), we find that jets in the subsolar magnetosheath mainly occur when this region is downstream of the quasi-parallel shock. As reported by Plaschke et al. (2013), the jets of this data set are more prevalent closer to the bow shock than to the magnetopause. According to our new results, the occurrence rate of jets downstream of the quasi-parallel shock is around 9 (6–14) times the corresponding rate downstream of the quasi-perpendicular shock. The rate seems to monotonically increase from the quasi-perpendicular shock toward the quasi-parallel shock. The analysis was done using one data point at the time of highest anti-sunward dynamic pressure (t_0) to represent each jet. For testing, we performed the same analysis using all jet interval data points, to ensure that short jets do not dominate the distribution. The results were not sensitive to this. As discussed in many previous studies (see Plaschke et al., 2018, and the references therein), jet formation seems to be linked to the nature of the quasi-parallel shock and the foreshock processes. Suggested formation processes that fit this picture include, e.g., bow shock ripples (Hietala et al., 2009; Hietala and Plaschke, 2013) and SLAMS (Karlsson et al., 2015; Palmroth et al., 2018).

We estimated how often jets hit the subsolar magnetopause during the three different IMF orientations using the model described by Plaschke et al. (2016). This model does not describe how jets are spatially distributed but only gives estimations of the total impact rates during given IMF conditions. One can make an assumption that the spatial distribution would follow the distribution of jets shown in Figure 11, but we do not know how the propagation of these jets changes when travelling toward the magnetopause. However, in Figure 12, we can see that the general trends of spatial occurrence are preserved close to the magnetopause in the Y_{GIPM}-direction. In addition, the results of Hietala and Plaschke (2013) indicated that jets are able to maintain their propagation direction quite well. As shown in Figure 16, jets are also able to penetrate through the magnetic pile-up layer during northward IMF.

Our results provide quantitative results on how often and where jets are expected to occur during different IMF orientations. Furthermore, estimations of the magnetopause impact rates, building on the previous results of Plaschke et al. (2016), tell us that jets are constantly hitting the magnetopause. This means that we can expect jet-induced effects on the magnetosphere to also be very common.

4.3 Possible effects of jets on magnetic reconnection

Magnetosheath jets exhibit magnetic fields that differ from the general fields of the subsolar magnetosheath plasma. The northward–southward orientation of the IMF controls the magnetic field B_Z strongly in the non-jet magnetosheath and moderately in jets. The B_Z distribution of jets does not broaden as much as the non-jet magnetosheath distribution when approaching the magnetopause. Therefore, while the non-jet magnetosheath is draped around the magnetopause, the jets seem to be able to hold their original magnetic field properties during their propagation.

When the IMF is southward, or more precisely when it has a southward component, the medians of the jet intervals and the non-jet magnetosheath are almost equal next to the magnetopause. However, the non-jet magnetosheath B_Z distribution has a larger spread than the jets. This means that the non-jet magnetosheath is more likely to have larger absolute values. From the perspective of increasing or decreasing magnetic shear at the magnetopause, the larger the absolute value of B_Z the better. When studying the minima and maxima of jet and non-jet intervals, we see that the variation in B_Z within jets is within the same scale or slightly smaller than the typical variation within the magnetosheath. Thus, during southward IMF, jets are not expected to statistically affect magnetopause reconnection, neither by suppressing or enhancing it. Reconnection is efficiently driven during southward IMF so any effects of jets are probably not very important.

During northward IMF, or when the IMF has a northward component, southward fields ($B_Z < 0$) next to the magnetopause are more common within jets than within the non-jet magnetosheath during similar IMF conditions. Here, 36 % of

jet interval measurements were southward as in comparison to 21 % ($\sigma = 0.021$ %) within the non-jet magnetosheath. Furthermore, when comparing jet intervals to similar duration non-jet intervals, only within 30 % ($\sigma = 4.3$ %) of the non-jet intervals the field was southward at any point. Remarkably, 73 % of the jet intervals had southward fields within them. Thus, it is clear that the variations within jets are not comparable to the typical variation within the magnetosheath. Therefore, we can conclude that during northward IMF, the magnetic field within jets is favorable for enhancing magnetopause reconnection due to jets exhibiting southward fields more often than the non-jet magnetosheath. Jets provide a way to bring southward fields to the vicinity of the magnetopause during northward IMF.

Nykyri et al. (2019) associated jets with southward B_Z observed during northward IMF to have triggered magnetopause reconnection. According to our results, jets with southward fields during northward IMF are not rare. In the future, we have to study the physical mechanisms resulting in these characteristics. We can start by studying how the results change with IMF obliquity (cone angle). Furthermore, we need to look at how the magnetic field changes within the jet interval and what is the duration of these southward minima: whether they are only brief changes in the field orientation or if they last longer. Jets may also affect magnetic shear at the magnetopause by indenting it, and therefore changing the magnetospheric field geometry, as proposed by (Hietala et al., 2018). On top of the effects of jets on the magnetic shear angle at this boundary, the high dynamic pressure of jets makes them also able to compress the magnetopause and make it thin enough for reconnection to occur. Observational evidence of such an event has already been provided by Hietala et al. (2018), although this was a special case since typically the magnetopause is notably thinner (e.g., Phan and Paschmann, 1996).

All in all, there are many ways how jets may possibly affect magnetopause reconnection. Their relative importance is yet to be studied, but as jets are not rare and, during northward IMF, jets often have magnetic fields favorable for enhancing reconnection, more research on this relationship should definitely be conducted.

5 Summary and conclusions

In this thesis, we studied how the orientation of the interplanetary magnetic field controls the occurrence of magnetosheath jets and their estimated magnetopause impact rates. The results of this aforementioned study have been published by Vuorinen et al. (2019). We studied the magnetic field within the jets themselves, specifically for the first time focusing on their $B_{Z,\mathrm{GSM}}$ distribution close to the subsolar magnetopause to understand whether jets could affect magnetic reconnection.

We find that the occurrence of jets downstream of the quasi-parallel shock is 9 times the occurrence downstream of the quasi-perpendicular shock. In the subsolar magnetosheath, during oblique IMF, the occurrence of jets grows monotonically from the quasi-perpendicular side toward the quasi-parallel side. Jets, especially smaller ones, are constantly hitting the subsolar magnetopause but the impact rates are the highest during low cone angle IMF when this region is downstream of the quasi-parallel shock. During these conditions, almost 60 jets per hour with sizes of $> 1\,R_{\mathrm{E}}$ perpendicular to their propagation direction hit the subsolar magnetopause. During unfavorable conditions, i.e., downstream of the quasi-perpendicular shock, such jets hit the subsolar magnetopause around 5 times per hour.

We found that the magnetic field within jets is statistically different compared to the non-jet magnetosheath magnetic field. We studied the magnetic field GSM B_Z component in detail as a function of relative position between the magnetopause and the bow shock. We found that jets seem to be able to preserve their magnetic field direction better than the non-jet magnetosheath. During southward IMF, the magnetic field in the non-jet magnetosheath itself has larger variations than the jets close to the magnetopause and jets are not expected to have a statistical impact on magnetopause reconnection. However, during northward IMF, when reconnection is generally suppressed at the subsolar magnetopause, the magnetic field within jets is statistically favorable for enhancing magnetopause reconnection as jets have southward fields more often than similar non-jet intervals. Remarkably, around 70 % of

jets close to the magnetopause exhibit southward fields when the IMF has a northward component, compared to around 30 % for similar magnetosheath intervals.

6 Outlook

In the future, we want to study the B_Z distribution of jets separately for the two hemispheres in order to see how the draping of the background magnetic field around the jets affects the results. We also need to investigate how the results change with different IMF cone angles as the draping patterns change with IMF obliquity. From the perspective of magnetopause reconnection, it is also important to study how long these intervals of southward B_Z within the jets are during northward IMF.

There is still plenty to be studied within the topic of magnetic properties and characteristics of magnetosheath jets. It would also be interesting to study how the turbulence of the IMF, i.e., variations in its direction and magnitude, affect the occurrence of magnetosheath jets. As jets are mainly observed downstream of the quasi-parallel shock with the extended foreshock region, we would assume that large variations in the IMF orientation may prevent a foreshock region from forming and thus affect the rippling of the bow shock and the possibly also the formation of jets.

Magnetosheath jets have become an active research topic in magnetospheric physics. They have been observed to be an important phenomenon for the dynamics of the bow shock-magnetosphere system. Jets will most likely continue to be linked to many observed processes and effects within the magnetosphere. Future studies will reveal whether these structures are inherent to all collisionless shocks in space.

7 Acknowledgements

This work was supported by the Jenny and Antti Wihuri Foundation and the Turku Collegium for Science and Medicine. We acknowledge NASA contract NAS5-02099 and V. Angelopoulos for use of data from the THEMIS mission and thank Ferdinand Plaschke for preparing the data set used in this thesis. The THEMIS and OMNI data are publicly available via, e.g., spedas.org.

References

Amata, E., Savin, S., Ambrosino, D., Bogdanova, Y., Marcucci, M., Romanov, S., and Skalsky, A.: High kinetic energy density jets in the Earth's magnetosheath: A case study, Planetary and Space Science, 59, 482–494, https://doi.org/10.1016/j.pss.2010.07.021, 2011.

Angelopoulos, V.: The THEMIS Mission, Space Science Reviews, 141, 5, https://doi.org/10.1007/s11214-008-9336-1, 2008.

Archer, M. O. and Horbury, T. S.: Magnetosheath dynamic pressure enhancements: occurrence and typical properties, Annales Geophysicae, 31, 319–331, https://doi.org/10.5194/angeo-31-319-2013, 2013.

Archer, M. O., Horbury, T. S., and Eastwood, J. P.: Magnetosheath pressure pulses: Generation downstream of the bow shock from solar wind discontinuities, Journal of Geophysical Research, 117, 1–13, https://doi.org/10.1029/2011JA017468, 2012.

Archer, M. O., Hartinger, M. D., and Horbury, T. S.: Magnetospheric "magic" frequencies as magnetopause surface eigenmodes, Geophysical Research Letters, 40, 5003–5008, https://doi.org/10.1002/grl.50979, 2013.

Archer, M. O., Hietala, H., Hartinger, M. D., Plaschke, F., and Angelopoulos, V.: Direct observations of a surface eigenmode of the dayside magnetopause, Nature Communications, 10, 615, https://doi.org/10.1038/s41467-018-08134-5, 2019.

Auster, H. U., Glassmeier, K. H., Magnes, W., Aydogar, O., Baumjohann, W., Constantinescu, D., Fischer, D., Fornacon, K. H., Georgescu, E., Harvey, P., Hillenmaier, O., Kroth, R., Ludlam, M., Narita, Y., Nakamura, R., Okrafka, K., Plaschke, F., Richter, I., Schwarzl, H., Stoll, B., Valavanoglou, A., and Wiedemann, M.: The THEMIS Fluxgate Magnetometer, Space Science Reviews, 141, 235–264, https://doi.org/10.1007/s11214-008-9365-9, 2008.

Balogh, A., Schwartz, S. J., Bale, S. D., Balikhin, M. A., Burgess, D., Horbury, T. S., Krasnoselskikh, V. V., Kucharek, H., Lembège, B., Lucek, E. A., Möbius, E., Scholer, M., Thomsen, M. F., and Walker, S. N.: Cluster at the Bow Shock: Introduction, Space Science Reviews, 118, 155–160, https://doi.org/10.1007/s11214-005-3826-1, 2005.

Bieber, J. W. and Stone, S. C.: Energetic electron bursts in the magnetopause electron layer and in interplanetary space, in: Magnetospheric Boundary Layers, edited by Battrick, B., Mort, J., Haerendel, G., and Ortner, J., vol. 148 of *ESA Special Publication*, pp. 131–135, European Space Agency, Paris, France, 1979.

Blanco-Cano, X., Omidi, N., and Russell, C. T.: Global hybrid simulations: Foreshock waves and cavitons under radial interplanetary magnetic field geometry, Journal of Geophysical Research: Space Physics (1978–2012), 114, https://doi.org/10.1029/2008JA013406, 2009.

Blanco-Cano, X., Kajdič, P., Omidi, N., and Russell, C. T.: Foreshock cavitons for different interplanetary magnetic field geometries: Simulations and observations, Journal of Geophysical Research: Space Physics (1978–2012), 116, https://doi.org/10.1029/2010JA016413, 2011.

Bothmer, V. and Daglis, I. A.: Introduction, in: Space Weather: Physics and Effects, edited by Bothmer, V. and Daglis, I. A., Springer-Verlag Berlin Heidelberg and Praxis Publishing, Berlin, Germany and Chichester, United Kingdom, 1st edition, 2007.

Bothmer, V. and Zhukov, A.: The Sun as the prime source of space weather, in: Space Weather: Physics and Effects, edited by Bothmer, V. and Daglis, I. A., Springer-Verlag Berlin Heidelberg and Praxis Publishing, Berlin, Germany and Chichester, United Kingdom, 1st edition, 2007.

Brown, L. D., Cai, T. T., and DasGupta, A.: Interval Estimation for a Binomial Proportion, Statistical Science, 16, 101–133, https://doi.org/10.1214/ss/1009213286, 2001.

Burgess, D. and Scholer, M.: Collisionless Shocks in Space Plasmas, Cambridge University Press, Cambridge, United Kingdom, 2015.

Cassak, P. A. and Fuselier, S. A.: Reconnection at Earth's Dayside Magnetopause, in: Magnetic Reconnection, edited by Gonzalez, W. and Parker, E., pp. 213–276, Springer International Publishing, Cham, Switzerland, 1st edition, https://doi.org/10.1007/978-3-319-26432-5, 2016.

Crosby, N. B.: Major radiation environments in the heliosphere and their implications for interplanetary travel, in: Space Weather: Physics and Effects, edited by Bothmer, V. and Daglis, I. A., Springer-Verlag Berlin Heidelberg and Praxis Publishing, Berlin, Germany and Chichester, United Kingdom, 1st edition, 2007.

Dimmock, A. P. and Nykyri, K.: The statistical mapping of magnetosheath plasma properties based on THEMIS measurements in the magnetosheath interplanetary medium reference frame, Journal of Geophysical Research: Space Physics, 118, 4963–4976, https://doi.org/10.1002/jgra.50465, 2013.

Dmitriev, A. V. and Suvorova, A. V.: Traveling magnetopause distortion related to a large-scale magnetosheath plasma jet: THEMIS and ground-based observations, Journal of Geophysical Research: Space Physics, 117, A08 217, https://doi.org/10.1029/2011JA016861, 2012.

Dmitriev, A. V. and Suvorova, A. V.: Large-scale jets in the magnetosheath and plasma penetration across the magnetopause: THEMIS observations, Journal of Geophysical Research: Space Physics, 120, 4423–4437, https://doi.org/10.1002/2014JA020953, 2015.

Eastwood, J. P., Lucek, E. A., Mazelle, C., Meziane, K., Narita, Y., Pickett, J., and Treumann, R. A.: The foreshock, Space Science Reviews, 118, 41–94, https://doi.org/10.1007/s11214-005-3824-3, 2005.

Eastwood, J. P., Hietala, H., Toth, G., Phan, T. D., and Fujimoto, M.: What Controls the Structure and Dynamics of Earth's Magnetosphere?, Space Science Reviews, 188, 251–286, https://doi.org/10.1007/s11214-014-0050-x, 2015.

Fairfield, D. H.: The ordered magnetic field of the magnetosheath, Journal of Geophysical Research (1896-1977), 72, 5865–5877, https://doi.org/10.1029/JZ072i023p05865, 1967.

Formisano, V.: The three-dimensional shape of the bow shock, Il Nuovo Cimento C, 2, 681–692, https://doi.org/10.1007/BF02558125, 1979.

Giacalone, J., Schwartz, S. J., and Burgess, D.: Observations of suprathermal ions in association with SLAMS, Geophysical Research Letters, 20, 149–152, https://doi.org/10.1029/93GL00067, 1993.

Gunell, H., Nilsson, H., Stenberg, G., Hamrin, M., Karlsson, T., Maggiolo, R., André, M., Lundin, R., and Dandouras, I.: Plasma penetration of the dayside magnetopause, Physics of Plasmas, 19, 072 906, https://doi.org/10.1063/1.4739446, 2012.

Gunell, H., Stenberg Wieser, G., Mella, M., Maggiolo, R., Nilsson, H., Darrouzet, F., Hamrin, M., Karlsson, T., Brenning, N., De Keyser, J., André, M., and Dandouras, I.: Waves in high-speed plasmoids in the magnetosheath and at the magnetopause, Annales Geophysicae, 32, 991–1009, https://doi.org/10.5194/angeo-32-991-2014, 2014.

Gutynska, O., Sibeck, D. G., and Omidi, N.: Magnetosheath plasma structures and their relation to foreshock processes, Journal of Geophysical Research: Space Physics, 120, 7687–7697, https://doi.org/10.1002/2014JA020880, 2015.

Hansteen, V. H.: Stellar winds and magnetic fields, in: Heliophysics: Plasma Physics of the Local Cosmos, edited by Schrijver, C. J. and Siscoe, G. L., pp. 225–255, Cambridge University Press, New York, United States, https://doi.org/10.1017/CBO9781107340657.010, 2009.

Hao, Y., Lembege, B., Lu, Q., and Guo, F.: Formation of downstream high-speed jets by a rippled nonstationary quasi-parallel shock: 2-D hybrid simulations, Journal of Geophysical Research: Space Physics, 121, 2080–2094, https://doi.org/10.1002/2015JA021419, 2016.

Hapgood, M.: Space physics coordinate transformations: A user guide, Planetary and Space Science, 40, 711–717, https://doi.org/10.1016/0032-0633(92)90012-D, 1992.

Heliophysics Science Division at NASA's GSFC: The Sun's Magnetic Field, https://helios.gsfc.nasa.gov/solarmag.html, accessed: April 11, 2019, 2012.

Hietala, H. and Plaschke, F.: On the generation of magnetosheath high-speed jets by bow shock ripples, Journal of Geophysical Research: Space Physics, 118, 7237–7245, https://doi.org/10.1002/2013JA019172, 2013.

Hietala, H., Laitinen, T. V., Andréeová, K., Vainio, R., Vaivads, A., Palmroth, M., Pulkkinen, T. I., Koskinen, H. E. J., Lucek, E. A., and Rème, H.: Supermagnetosonic Jets behind a Collisionless Quasiparallel Shock, Physical Review Letters, 103, 245 001, https://doi.org/10.1103/PhysRevLett.103.245001, 2009.

Hietala, H., Partamies, N., Laitinen, T. V., Clausen, L. B. N., Facskó, G., Vaivads, A., Koskinen, H. E. J., Dandouras, I., Rème, H., and Lucek, E. A.: Supermagnetosonic subsolar magnetosheath jets and their effects: from the solar wind to the ionospheric convection, Annales Geophysicae, 30, 33–48, https://doi.org/10.5194/angeo-30-33-2012, 2012.

Hietala, H., Phan, T. D., Angelopoulos, V., Oieroset, M., Archer, M. O., Karlsson, T., and Plaschke, F.: In Situ Observations of a Magnetosheath High-Speed Jet Triggering Magnetopause Reconnection, Geophysical Research Letters, 45, 1732–1740, https://doi.org/10.1002/2017GL076525, 2018.

Kallenrode, M.-B.: Space Physics, Springer-Verlag Berlin Heidelberg, Germany, 1998.

Karlsson, T., Brenning, N., Nilsson, H., Trotignon, J.-G., Vallières, X., and Facsko, G.: Localized density enhancements in the magnetosheath: Three-dimensional morphology and possible importance for impulsive penetration, Journal of Geophysical Research: Space Physics, 117, A03 227, https://doi.org/10.1029/2011JA017059, 2012.

Karlsson, T., Kullen, A., Liljeblad, E., Brenning, N., Nilsson, H., Gunell, H., and Hamrin, M.: On the origin of magnetosheath plasmoids and their relation to magnetosheath jets, Journal of Geophysical Research: Space Physics, 120, 7390–7403, https://doi.org/10.1002/2015JA021487, 2015.

King, J. H. and Papitashvili, N. E.: Solar wind spatial scales in and comparisons of hourly Wind and ACE plasma and magnetic field data, Journal of Geophysical Research: Space Physics (1978–2012), 110, https://doi.org/10.1029/2004JA010649, 2005.

Koskinen, H.: Johdatus plasmafysiikkaan ja sen avaruussovellutuksiin, Limes ry, Helsinki, Finland, 2nd edition, 2011.

Lee, S. H., Sibeck, D. G., Hwang, K., Wang, Y., Silveira, M. V. D., Fok, M., Mauk, B. H., Cohen, I. J., Ruohoniemi, J. M., Kitamura, N., Burch, J. L., Giles, B. L., Torbert, R. B., Russell, C. T., and Lester, M.: Inverse energy dispersion of energetic ions observed in the magnetosheath, Geophysical Research Letters, 43, 7338–7347, https://doi.org/10.1002/2016GL069840, 2016.

Lin, Y., Lee, L. C., and Yan, M.: Generation of dynamic pressure pulses downstream of the bow shock by variations in the interplanetary magnetic field orientation, Journal of Geophysical Research: Space Physics, 101, 479–493, https://doi.org/10.1029/95JA02985, 1996a.

Lin, Y., Swift, D. W., and Lee, L. C.: Simulation of pressure pulses in the bow shock and magnetosheath driven by variations in interplanetary magnetic field direction, Journal of Geophysical Research: Space Physics, 101, 27 251–27 269, https://doi.org/10.1029/96JA02733, 1996b.

Liu, T. Z., Hietala, H., Angelopoulos, V., Omelchenko, Y., Roytershteyn, V., and Vainio, R.: THEMIS Observations of Particle Acceleration by a Magnetosheath Jet-Driven Bow Wave, Geophysical Research Letters, 46, 7929–7936, https://doi.org/10.1029/2019GL082614, 2019.

Lucek, E. A., Horbury, T. S., Dandouras, I., and Re, H.: Cluster observations of the Earth's quasi-parallel bow shock, Journal of Geophysical Research, 113, 1–11, https://doi.org/10.1029/2007JA012756, 2008.

MathWorks^{TM}: Create Arrays of Random Numbers, `https://se.mathworks.com/help/matlab/math/create-arrays-of-random-numbers.html`, accessed: September 13, 2019, 2018.

McFadden, J. P., Carlson, C. W., Larson, D., Ludlam, M., Abiad, R., Elliott, B., Turin, P., Marckwordt, M., and Angelopoulos, V.: The THEMIS ESA Plasma Instrument and In-flight Calibration, Space Science Reviews, 141, 277–302, https://doi.org/10.1007/s11214-008-9440-2, 2008.

Merka, J. and Szabo, A.: Bow shock's geometry at the magnetospheric flanks, Journal of Geophysical Research: Space Physics (1978–2012), 109, https://doi.org/10.1029/2004JA010567, 2004.

Merka, J., Szabo, A., Slavin, J. A., and Peredo, M.: Three-dimensional position and shape of the bow shock and their variation with upstream Mach numbers and interplanetary magnetic field orientation, Journal of Geophysical Research: Space Physics, 110, 1–13, https://doi.org/10.1029/2004JA010944, 2005.

NOAA: Space Weather Prediction Center: Solar Cycle Progression, `https://www.swpc.noaa.gov/products/solar-cycle-progression`, accessed: October 21, 2019, 2019.

Nykyri, K., Bengtson, M., Angelopoulos, V., Nishimura, Y., and Wing, S.: Can Enhanced Flux Loading by High-Speed Jets Lead to a Substorm? Multipoint Detection of the Christmas Day Substorm Onset at 08:17 UT, 2015, Journal of Geophysical Research: Space Physics, 124, 4314–4340, https://doi.org/10.1029/2018JA026357, 2019.

Němeček, Z., Šafránková, J., Přech, L., Sibeck, D. G., Kokubun, S., and Mukai, T.: Transient flux enhancements in the magnetosheath, Geophysical Research Letters, 25, 1273–1276, https://doi.org/10.1029/98GL50873, 1998.

Němeček, Z., Šafránková, J., Přech, L., Zastenker, G. N., Paularena, K., and Kokubun, S.: Magnetosheath study: INTERBALL observation, Advances in Space Research, 25, 1511–1516, https://doi.org/10.1016/S0273-1177(99)00663-8, 2000.

Palmroth, M., Hietala, H., Plaschke, F., Archer, M., Karlsson, T., Blanco-Cano, X., Sibeck, D., Kajdič, P., Ganse, U., Pfau-Kempf, Y., Battarbee, M., and Turc, L.: Magnetosheath jet properties and evolution as determined by a global hybrid-Vlasov simulation, Annales Geophysicae, 36, 1171–1182, https://doi.org/10.5194/angeo-36-1171-2018, 2018.

Parker, E. N.: Dynamics of the Interplanetary Gas and Magnetic Fields., Astrophysical Journal, 128, 664, https://doi.org/10.1086/146579, 1958.

Phan, T. D. and Paschmann, G.: Low-latitude dayside magnetopause and boundary layer for high magnetic shear: 1. Structure and motion, Journal of Geophysical Research: Space Physics, 101, 7801–7815, https://doi.org/10.1029/95JA03752, 1996.

Phan, T. D., Paschmann, G., Baumjohann, W., Sckopke, N., and Lühr, H.: The magnetosheath region adjacent to the dayside magnetopause: AMPTE/IRM observations, Journal of Geophysical Research: Space Physics, 99, 121–141, https://doi.org/10.1029/93JA02444, 1994.

Plaschke, F. and Hietala, H.: Plasma flow patterns in and around magnetosheath jets, Annales Geophysicae, 36, 695–703, https://doi.org/10.5194/angeo-36-695-2018, 2018.

Plaschke, F., Hietala, H., and Angelopoulos, V.: Anti-sunward high-speed jets in the subsolar magnetosheath, Annales Geophysicae, 31, 1877–1889, https://doi.org/10.5194/angeo-31-1877-2013, 2013.

Plaschke, F., Hietala, H., Angelopoulos, V., and Nakamura, R.: Geoeffective jets impacting the magnetopause are very common, Journal of Geophysical Research A: Space Physics, 121, 3240–3253, https://doi.org/10.1002/2016JA022534, 2016.

Plaschke, F., Hietala, H., Archer, M., Blanco-Cano, X., Kajdič, P., Karlsson, T., Lee, S. H., Omidi, N., Palmroth, M., Roytershteyn, V., Schmid, D., Sergeev, V., and Sibeck, D.: Jets Downstream of Collisionless Shocks, Space Science Reviews, 214, 81, https://doi.org/10.1007/s11214-018-0516-3, 2018.

Plaschke, F., Jernej, M., Hietala, H., and Vuorinen, L.: On the alignment of velocity and magnetic fields within magnetosheath jets, Annales Geophysicae Discussions, 2019, 1–13, https://doi.org/10.5194/angeo-2019-92, accepted, 2020.

Press, W. H., Teukolsky, S. A., Vetterling, W. T., and Flannery, B. P.: Numerical Recipes: The Art of Scientific Computing, Cambridge University Press, New York, USA, 3rd edition, 2007.

Ross, S.: Chapter 4 – Generating Discrete Random Variables, in: Simulation, edited by Ross, S., pp. 47–68, Academic Press, 5th edition, https://doi.org/10.1016/B978-0-12-415825-2.00004-8, 2013.

Savin, S., Amata, E., Zelenyi, L., Budaev, V., Consolini, G., Treumann, R., Lucek, E., Safrankova, J., Nemecek, Z., Khotyaintsev, Y., Andre, M., Buechner, J., Alleyne, H., Song, P., Blecki, J., Rauch, J. L., Romanov, S., Klimov, S., and Skalsky, A.: High energy jets in the Earth's magnetosheath: Implications for plasma dynamics and anomalous transport, Journal of Experimental and Theoretical Physics Letters, 87, 593–599, https://doi.org/10.1134/S0021364008110015, 2008.

Savin, S., Amata, E., Budaev, V., Zelenyi, L., Kronberg, E. A., Buechner, J., Safrankova, J., Nemecek, Z., Blecki, J., Kozak, L., Klimov, S., Skalsky, A., and Lezhen, L.: On nonlinear cascades and resonances in the outer magnetosphere, Journal of Experimental and Theoretical Physics Letters, 99, 16–21, https://doi.org/10.1134/S002136401401010X, 2014.

Schwartz, S. J.: Magnetic field structures and related phenomena at quasi-parallel shocks, Advances in Space Research, 11, 231–240, https://doi.org/10.1016/0273-1177(91)90039-M, 1991.

Schwartz, S. J. and Burgess, D.: Quasi-parallel shocks: A patchwork of three-dimensional structures, Geophysical Research Letters, 18, 373–376, https://doi.org/10.1029/91GL00138, 1991.

Shue, J.-H., Song, P., Russell, C. T., Steinberg, J. T., Chao, J. K., Zastenker, G., Vaisberg, O. L., Kokubun, S., Singer, H. J., Detman, T. R., and Kawano, H.: Magnetopause location under extreme solar wind conditions, Journal of Geophysical Research: Space Physics, 103, 17 691–17 700, https://doi.org/10.1029/98JA01103, 1998.

SOHO (ESA & NASA): Gallery, `https://sohowww.nascom.nasa.gov/gallery/images/magfield.html`, accessed: January 15, 2020.

Spreiter, J. R., Summers, A. L., and Alksne, A. Y.: Hydromagnetic flow around the magnetosphere, Planetary and Space Science, 14, 223–253, https://doi.org/10.1016/0032-0633(66)90124-3, 1966.

Trattner, K. J., Mulcock, J. S., Petrinec, S. M., and Fuselier, S. A.: Probing the boundary between antiparallel and component reconnection during southward interplanetary magnetic field conditions, Journal of Geophysical Research: Space Physics (1978–2012), 112, https://doi.org/10.1029/2007JA012270, 2007.

Verigin, M. I., Tátrallyay, M., Erdős, G., and Kotova, G. A.: Magnetosheath – Interplanetary medium reference frame: Application for a statistical study of mirror type waves in the terrestrial plasma environment, Advances in Space Research, 37, 515–521, https://doi.org/10.1016/j.asr.2005.03.042, 2006.

Vuorinen, L., Hietala, H., and Plaschke, F.: Jets in the magnetosheath: IMF control of where they occur, Annales Geophysicae, 37, 689–697, https://doi.org/10.5194/angeo-37-689-2019, 2019.

Wang, B., Nishimura, Y., Hietala, H., Lyons, L., Angelopoulos, V., Plaschke, F., Ebihara, Y., and Weatherwax, A.: Impacts of Magnetosheath High-Speed Jets on the Magnetosphere and Ionosphere Measured by Optical Imaging and Satellite Observations, Journal of Geophysical Research: Space Physics, 123, 4879–4894, https://doi.org/10.1029/2017JA024954, 2018.

Yamada, M., Kulsrud, R., and Ji, H.: Magnetic reconnection, Reviews of Modern Physics, 82, 603–664, https://doi.org/10.1103/RevModPhys.82.603, 2010.